The Impact of Convection on the Transport and Removal of Dust Aerosols

Author:

Kathryn SAUTER

A thesis submitted in partial fulfillment of

the requirements for the degree of

Master of Science

(Atmospheric and Oceanic Sciences)

at the

UNIVERSITY OF WISCONSIN-MADISON

September 2016

Thesis Declaration and Approval

I, Kathryn SAUTER, declare that this thesis titled 'The Impact of Convection on the Transport and Removal of Dust Aerosols' and the work presented in it are my own.

Kathryn SAUTER
_____   _____   _____
Author   Signature   Date

I hereby approve and recommend for acceptance this work in partial fulfillment of the requirements for the degree of Master of Science:

Tristan S. L'ECUYER
_____   _____   _____
Committee Chair   Signature   Date

Bradley R. PIERCE
_____   _____   _____
Faculty Member   Signature   Date

Daniel J. VIMONT
_____   _____   _____
Faculty Member   Signature   Date

Abstract

The Impact of Convection on the Transport and Removal of Dust Aerosols

by Kathryn SAUTER

The distribution of mineral dust aerosols that originate from the Saharan Desert and sweep across the tropical Atlantic Ocean can significantly impact climate processes in the region. Dust loadings have been estimated to double in the 20th century, enhancing the impacts of these processes (Mahowald et al., 2010), particularly during drought events (Prospero and Lamb 2003). The Cloud-Aerosol Lidar and Infrared Pathfinder Satellite Observations (CALIPSO) mission was launched in April 2006 as a part of the A-Train constellation in order to gain a better understanding of the role that aerosols and clouds play in the complex climate system (Winker et al. 2006, 2007). The ability to assess the vertical and spatial transport of dust across the Atlantic Ocean using CALIPSO aerosol retrievals provides valuable insights into the effects of dust aerosols on the Earth's climate system. This study couples in-situ observations of dust storm events with aerosol optical depth from the polar orbiting CALIPSO ground track and the Pathfinder Atmospheres Extended (PATMOS-x) cloud product dataset to constrain the transport and redistribution of dust aerosols over the tropical Atlantic Ocean owing to the passage of convection. Cloud top temperature, cloud optical thickness, and cloud top size are further used to quantify the sensitivity of wet deposition to the intensity of tropical convection. It is conjectured that when there are more convective clouds present,

more dust will be removed from the atmosphere. Preliminary results provide evidence that convection both reduces downstream dust optical depths and occasionally transports dust to higher altitudes than the main Saharan dust layer. These redistribution and scavenging effects have implications for direct and indirect impacts of dust on radiation balance both locally and downstream of the convection. Further analysis of these complementary datasets may offer new revelations into aerosol-cloud climate interactions.

"You have brains in your head. You have feet in your shoes. You can steer yourself in any direction you choose"

-Dr. Seuss

Acknowledgements

First and foremost, I would like to thank my advisor, Tristan L'Ecuyer, for all of the support and encouragement throughout this research project. He has provided guidance and direction in multiple aspects in order for me to grow into a well-rounded scientist. I could not have asked for a more enthusiastic, dedicated mentor to work with throughout my graduate studies.

I would also like to individually thank Norm Wood, Ethan Nelson and Alex Matus for all of the programming help from the beginning of this project. Without their direction, this research would not be where it is today. I would also like to thank Steve Wanzong and Andy Heidinger for all the data processing for PATMOS-x data. Gratitude and thank you also goes out to Brad Pierce, Sue Van Den Heever and her research group, Cindy Twohy and Dan Vimont for providing valuable input and feedback in order to improve this research.

My research group and departmental colleagues deserve superior recognition as well for all of the support they have given during the past couple of years through out classes and research life. I am extremely grateful to be amongst some of the most intelligent and driven group of young scientists.

A very special thank you goes to my family and friends who have unconditionally loved and supported me throughout this entire journey. Without them by my side, I would not be in the position that I am today.

Contents

List of Figures

List of Tables

Abbreviations

ACHA	**AWG** **C**loud **H**eight **A**lgorithm
AERONET	**Ae**rosol **Ro**botic Network
AEW	**A**frican **E**asterly **W**ave
AVHRR	**A**dvanced **V**ery **H**igh **R**esolution **R**adiometer
AWG	**A**lgorithm **W**orking **G**roup
CAD	**C**loud **A**erosol **D**iscrimination
CALIPSO	**C**loud **A**erosol **L**idar **I**nfrared **P**athfinder **S**atellite **O**bservation
CALIOP	**C**loud **A**erosol **Li**dar with **O**rthogonal **P**olarization
CCN	**C**loud **C**ondensation **N**uclei
CESM	**C**ommunity **E**arth for **S**ystem Model
CPR	**C**loud **P**rofiling **R**adar
CRM	**C**loud **R**esolving **M**odel
dBZ	**d**eci**B**els relative to radar reflectivity
DCOMP	**D**aytime **C**loud **O**ptical **M**icrophysical **P**roperties
DDA	**D**iscrete **D**ipole **A**pproximation
ECMWF	**E**uropean **C**enter for Medium range **W**eather **F**orecasts
EUMETSAT	**EU**ropean organisation for the exploitation of **MET**eorological **SAT**ellites
FS	**F**ootprint **S**ize
GAC	**G**lobal **A**rea **C**overage
GHz	**G**iga**H**ert**z**
GOES	**G**eostationary **O**perational **E**nvironmental **S**atellite

IGBP	**I**nternational **G**eosphere- **B**iosphere **P**rogramme
IIR	**I**maging **I**nfrared **R**adiometer
IN	**I**ce **N**uclei
IPCC	**I**ntergovernmental **P**anel on **C**limate **C**hange
ITCZ	**I**nter **T**ropical **C**onvergence **Z**one
K	**K**elvin
km	**k**ilometer
m	**m**eter
MCS	**M**esoscale **C**onvective **S**ystem
mph	**m**iles **p**er **h**our
mb	**m**illi**b**ar
MODIS	**MOD**erate resolution **I**maging **S**pectrometer
NAMMA	**N**AS**A**s **A**frican **M**onsoon **M**ultidisiplinary **A**nalysis
nm	**n**anometer
NASA	**N**ational **A**eronautics and **S**pace **A**dministration
NCAR	**N**ational **C**enter for **A**tmospheric **R**esearch
NOAA	**N**ational **O**ceanic and **A**tmospheric **A**dministration
OCO-2	**O**rbiting **C**arbon **O**bservatory - **2**
PARASOL	**P**olarization and **A**nisotropy of **R**eflectance for **A**tmospheric **S**cience coupled with **O**bservations from a **L**idar
PATMOS-x	**PAT**hfinder **ATMOS**pheres E**x**tended
RAMS	**R**egional **A**tmospheric **M**odeling **S**ystem
SAL	**S**aharan **A**ir **L**ayer
SHADE	**S**a**HA**ran **D**ust **E**xperiment
sr	**s**teradian
TRMM	**T**ropical **R**ainfall **M**easuring **M**ission
um	**m**icrometer
us	**m**icrosecond
WFC	**W**ide **F**ield **C**amera

Chapter 1

Introduction

1.1 Importance of Mineral Dust Aerosols

Atmospheric aerosols are tiny particles that are globally dispersed and provide an array of complications when studying Earth's climate processes. Mineral dust aerosols contribute a significant portion of the overall aerosol mass both horizontally and vertically in the atmosphere, and encompass an extensive area of Earth. Dust is predominately generated from continents, with the Saharan Desert being the largest contributor of dust transport across the tropical Atlantic Ocean (Liu et al., 2012). Annual dust emissions from Northern Africa are in the range of 300-1600 teragrams (Tg) /year and account for 60-70% of global dust emissions (Rodríguez et al., 2011). Dust plumes are able to disperse along thousands of kilometers from the source and are transported westward by the northeast trade winds from the Saharan Desert across the Atlantic Ocean. This region contains an elevated layer of dust-laden air
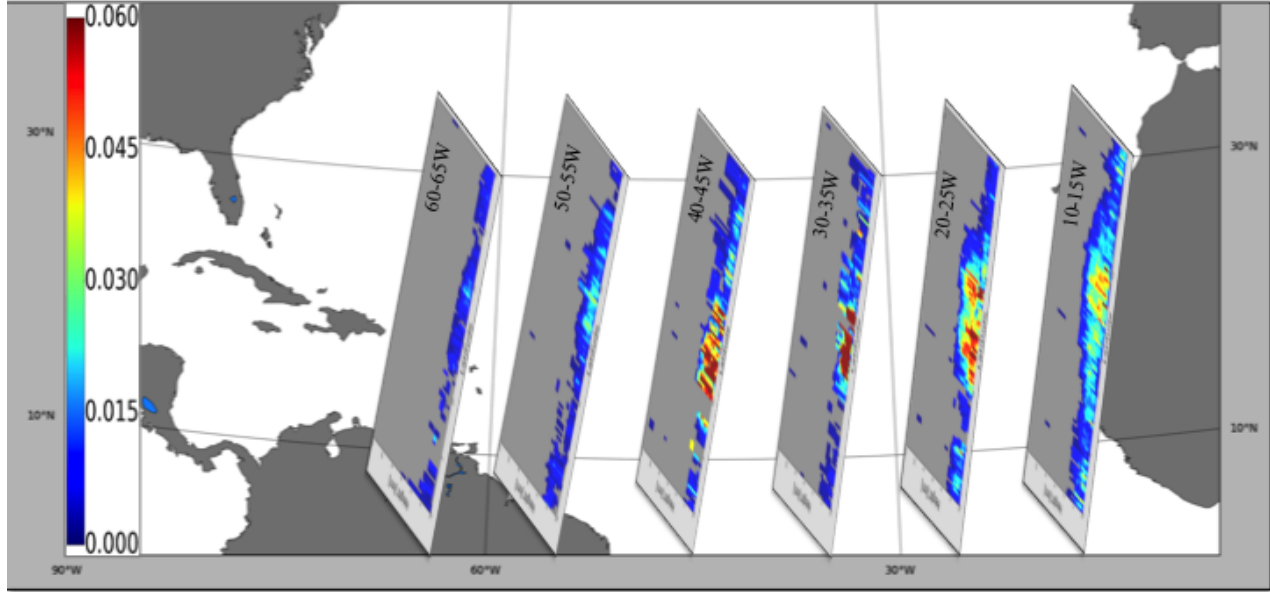
FIGURE 1.1: Aerosol Optical Depth for dust and polluted dust averaged over one month in October 2008 at 0°N - 30°N for 10W-15W, 20W-25W, 30W-35W, 40W-45W, 50W-55W and 60W-65W.

called the Saharan Air Layer (SAL) (Liu et al., 2008). The SAL tends to be stable and is a mixture of hot, dry air and mineral dust from the Saharan Desert that extends vertically from approximately .19 kilometers (km) - 1.8km and horizontally across the tropical Atlantic Ocean from 5.5km to about 7000km. Dust layers in the SAL can be visualized through satellite observations as illustrated by Figure **??** that shows average dust aerosol optical depth for October 2008 from Cloud Aerosol Lidar and Infrared Pathfinder Satellite Observations (CALIPSO). These cross sections illustrate how the depth and amount of dust decreases as a function of distance from the source region. Dunion and Velden (2004), Chen et al. (2011), Prospero and Nees (1977) showed that the mass mean diameter of dust aerosols decreases

with distance from the source region reaching typical values less than 10 micrometers (um) at long ranges. Individual dust particles can last anywhere between one hour for larger particles and several years for stratospheric particles (Tegen and Fung, 1994).

Strong seasonal cycles of dust in the vertical extent are present in the SAL, with the densest layers occurring in the high subtropical latitudes (15°N-30°N) during the summer and the least in the low tropical latitudes (0°N-10°N) in the winter (Liu et al., 2008, Rodríguez et al., 2011). Dust particles in the SAL are generally located between 2km and 4km above the surface, although there are particles that are lifted to 6km and above (Liu et al., 2008, Zipser et al., 2009). Northern and southern shifts are also present in the dust bands due to the seasonal movement of the Intertropical Convergence Zone (ITCZ) (Liu et al., 2012). During the summer, the ITCZ migrates northward allowing for more easterly airflow patterns in the tropical Atlantic Ocean, therefore causing larger amounts of dust to be transported westward across the ocean to the Caribbean. The ITCZ shifts southward during the northern hemispheric winter causing the airflow to be more northeasterly and dust transport to migrate further towards South America (Perry et al., 1997).

1.2   Climate Effects of Mineral Dust Aerosols

The large abundance of dust in the atmosphere from the SAL alters the climate system through a variety of complex processes (Klüser et al., 2008, Ramanathan et al., 2001, Rosenfeld et al., 2001)). Understanding these processes is critical for reducing the uncertainty associated with dust sources and sinks, long-range transport and the effects of dust particles on clouds

and radiation (Sokolik et al., 2001), **?**. Due to changes in atmospheric temperatures, land use practices and precipitation amounts, the amount of dust loading from the Saharan Desert is predicted to increase in the future, further creating ambiguity among the interactions between clouds and radiation (IPCC 2007).

One of the largest uncertainties in predicting global climate change is the radiative forcing of aerosols. Aerosols can alter atmospheric dynamics and thermodynamics (Quijano et al., 2000). Karyampudi and Carlson (1988) showed that a warmer and deeper SAL, an enhanced midlevel easterly jet and a reduction in equatorial convection all result from radiative heating by dust particles. Dust aerosols impact the radiation budget directly by virtue of scattering and absorbing, and can exert either a warming or cooling effect on the climate (Liu et al., 2008). Solar and radiative forcings at the top of the atmosphere can have either a positive or negative radiative effect depending on the cloud albedo (Sokolik et al., 2001), while dust aerosols can have a warming effect by reducing the longwave emission from the surface (Sokolik and Toon, 1998).

Dust particles also change cloud microphysical properties by acting as cloud condensation nuclei (CCN). Clouds containing more CCN lead to an increase in the number of cloud droplets, which lowers the collision coalescence rate by having smaller droplets and reduces precipitation efficiency (Khain et al., 2005, Rosenfeld et al., 2001). This decrease in efficiency within individual clouds also allows for weakened updraft strengths leading to more vigorous convection from greater amounts of latent heat (Andreae et al., 2004, Khain et al., 2005). Cloud lifetimes are also lengthened because smaller droplets are suspended in clouds longer

(Klüser and Holzer-Popp, 2010). Herbener et al. (2014) found that increasing dust aerosol concentrations increased the storm intensity, while the storm size decreased. An increase in CCN also leads to an increase in cloud albedo, causing a cooling effect from additional solar radiation being reflected back to space (Twomey, 1974).

Dust aerosols can further behave as effective ice nuclei (IN), as shown in a study by DeMott et al. (2010), further adjusting microphysical and radiative cloud properties, latent heating and precipitation rates (DeMott et al., 2003). Dust acting as ice nuclei has been observed to be present at higher levels in the atmosphere, which is of critical importance in determining ice phase transitions in cold clouds because dust IN leads to early freezing of cloud drops, thus increasing cloud updrafts and cold rain precipitation (DeMott et al., 2003, Jenkins et al., 2008). A study using field campaign measurements by Twohy (2015) indicated that dust was the most prevalent aerosol type located in cirrus anvil clouds, and were frequently mixed with hygroscopic material suggesting the dust originated in the SAL as opposed to the marine boundary layer.

Moreover, convective cloud properties are affected by aerosol loadings such as cloud cover, height and anvil portions. Cloud fraction increases while cloud top pressure and cloud effective radius both decrease as the dust layer is enhanced. Dust is typically ingested into Tropical Storms as they move through the SAL, further altering tropical storm characteristics (Twohy, 2015). Recently, there has been great effort made in understanding the interactions between convective clouds and aerosols. Dunion and Velden (2004) found that the SAL is likely to suppress Atlantic Tropical Cyclone activity by bringing dry, stable air into the storm,

thereby enhancing local vertical wind shear through the midlevel easterly jet and increasing the trade wind inversion in the Atlantic causing a stable environment. Rosenfeld et al. (2001) presented statistical evidence supporting this hypothesis. A study on the influence of aerosols on hurricanes by Carrio and Cotton (2011) concluded that the impact of aerosols on tropical storm genesis and intensity was due to the strength of the cold-pools, where an increased amount of CCN produced altered storm characteristics. This leads to a more widespread area of cold pools, blocking the flow of energy to the storm, ultimately inhibiting storm intensity.

Finally, mineral dust has a strong influence on marine biogeochemical processes through the transformation of ocean productivity because of the large concentration of iron and other restrictive nutrients in dust particles such as phosphorus (DeMott et al., 2003, Fung et al., 2000). Since many open oceans are deficient in large amounts of iron, adding iron-laden dust particles to the oceans surface will increase phytoplankton growth over 30-40% of the oceans, particularly in high-nitrate, low-chlorophyll regions (Martin et al., 1991, Martin and Gordon, 1988, Moore et al., 2004). Dust can be deposited to the oceans surface as a result of precipitating events (wet deposition) and through turbulent mixing and gravitational settling (dry deposition) (Mahowald et al., 2010). The consequence of the effects of mineral dust on marine biogeochemical processes comes with an adjustment of the carbon cycle, where a significant decrease in oceanic uptake of carbon dioxide could result in a positive feedback to global warming (Moore et al., 2006).

1.3   Interactions Between Mineral Dust Aerosols and Convection

The impact of dust aerosols on convective clouds has been investigated extensively, while the effect of convection on the dust layer is much less studied. Evan et al. (2006) suggested that the SAL acts as a control on Tropical Atlantic cyclone activity, although also implied changes in the dust loadings that are within the SAL itself. The goal of this research is to focus on the implications of convective activity in the tropical Atlantic Ocean for the transport of Saharan dust. Our main objectives are to determine the amount of dust that is removed from the atmosphere and deposited to the ocean through wet deposition processes from a variety of convective storm systems. We are particularly interested in mesoscale convective systems (MCSs), which are the dominant systems for transporting water vapor and energy vertically into the atmosphere (Tobin et al., 2012). These systems can be individual cells contributing to a squall line or mesoscale complex, or grouped together forming larger superclusers (Houze, 2004, Mapes, 1993). MCSs have a variety of cloud and precipitation structures that include areas of convective and stratiform clouds and precipitation. These systems develop mesoscale circulations as they mature, indicating their ability to move the dust layer throughout the atmosphere (Houze Jr, 2014).

MCSs and their contributing elements can be identified and classified into several categories through a multitude of meteorological parameters including area of cloud cover, cloud top temperatures and cloud top heights. Houze Jr (2014) suggested that an area of convection

rarely exceeds 2000-3000km^2, but the stratiform precipitation area can exceed 40,000km^2. Houze Jr and Cheng (1977) divided clouds into four categories based on area coverage with cumulus having an area of 1-10^2 km^2, mesoscale as 10^2-10^5 km^2, cloud clusters as 10^5-10^6 km^2 and synoptic scale cloud cover having an area greater than 10^6 km^2. Mapes and Houze Jr (1993) examined areas of cloudiness with blackbody temperatures less than a specific threshold, referred to as cloud clusters, and implemented a very cold threshold of 208 kelvin (K) and a moderately cold threshold of 235K to identify the clusters. Additional studies by Arkin (1979), Richards and Arkin (1981) and Arkin and Meisner (1987) used a 235K threshold as well for identifying the best linear regression between cloud clusters and rainfall. Williams and Houze Jr (1987) used a 213K threshold for identifying these cloud clusters, while Fu et al. (1990) used 215K and 267K for identifying tropical deep convective clouds and cirrus anvil clouds, respectively. In a study using the Tropical Rainfall Measuring Mission (TRMM) by Alcala and Dessler (2002), reflectivity tops that exceeded 10km were termed deep convection, where tops greater than 14km were classified as overshooting convection. The diversity of thresholds that are used in the numerous studies presented above indicates the dynamic nature of convection, particularly in larger systems, as identified by chosen thresholds from the Pathfinder Atmospheres Extended (PATMOS-x) cloud product datasets.

1.4   Research Objectives

This research concentrates on where the convective storms and systems redistribute the dust in the atmosphere and how convection has changed the vertical distribution of dust. Dust particles are highly variable in space and time, thus making it difficult to actually quantify

their physical distribution (Tegen and Fung, 1994). As mineral dust is the most prevalent aerosol type in the tropical Atlantic Ocean, it represents a significant factor in determining the interactions between clouds and aerosol in this region. This study uses a combination of polar orbiting and geostationary observations in order to generate composites of aerosol optical depth as a function of time before and after convection has passed. The datasets will be collocated together in order to combine aerosol layer information and a suite of cloud products. By creating a convective algorithm from this combined information, the aerosol layer around typical convective life cycles can be traced through time. These observational results will be used to evaluate transport and deposition simulated by cloud resolving models (CRMs) to assess how well the model reproduces where, how and the amount of dust that has been transported and redistributed by convection, as well as what the effects of the removal and redistribution of dust on ocean fertilization and indirect and direct radiative effects. This research embraces NASA's goal of utilizing Earth's observation systems to better provide estimates and knowledge of important processes in the Earth's climate system. The results of this research are expected to contribute to an improved understanding of how convection interacts with the dust layer, interpretation of how a variety of convective storm systems interact with the transport and redistribution of dust and, more broadly, aid in reducing the uncertainty in cloud aerosol interactions, ultimately causing further changes in climate.

Chapter 2

Datasets

2.1 Introduction

To provide observational evidence for the impacts of convection on Saharan dust, this analysis was completed using a combination of polar orbiting and geostationary satellite data and products. CloudSat measures reflectivity from which cloud top, cloud properties, and associated fluxes and heating rates are derived, while the Cloud-Aerosol Lidar and Infrared Pathfinder Satellite Observation (CALIPSO) instrument provides horizontal and vertical profiles of aerosol optical depth and aerosol type. Cloud top temperature, cloud optical depth and cloud top height were detected using the PATMOS-x dataset. A description of all products and satellites used for each dataset are discussed in this section.
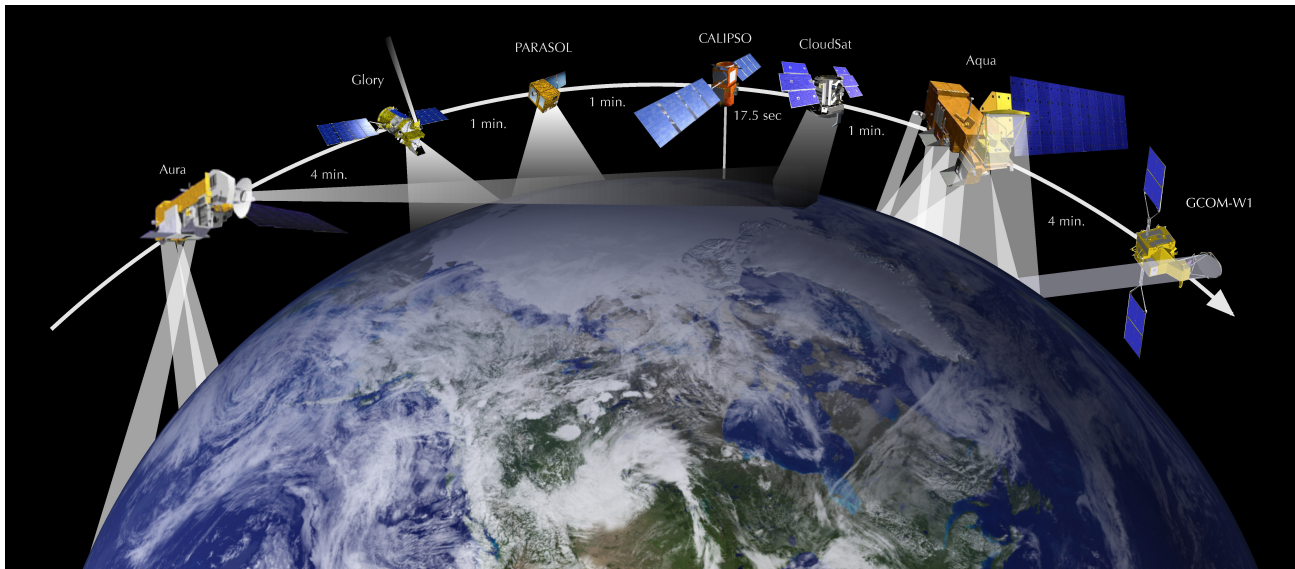
FIGURE 2.1: A-Train satellite constellation including time differences between each satellite.

2.2 CloudSat and CALIPSO

Launched in April 2006, CloudSat and CALIPSO are two spacecraft that are a part of the sun-synchronous, polar orbiting, Afternoon Train (A-Train) satellite constellation (L'Ecuyer and Jiang, 2010). The A-Train constellation, shown in Figure **??**, is comprised of six satellites including the Earth Observing Systems (EOS) Aqua and Aura, CloudSat, CALIPSO, Orbiting Carbon Observatory 2 (OCO-2) and Polarization and Anisotropy of Reflectance for Atmospheric Science coupled with Observations from a Lidar (PARASOL). The spacecraft fly at an altitude of 690 km with twice daily equatorial crossing times at approximately 01:30 and 13:30 local time and a 16 day repeating cycle (Stephens et al., 2002, Yu et al., 2010). The synergy of sensors aboard the A-Train satellites permit exceptional observations of the Earth's climate system and insight into the climate variability indicative of the influence of clouds. When used together, CloudSat and CALIPSO provide a wealth of high quality information
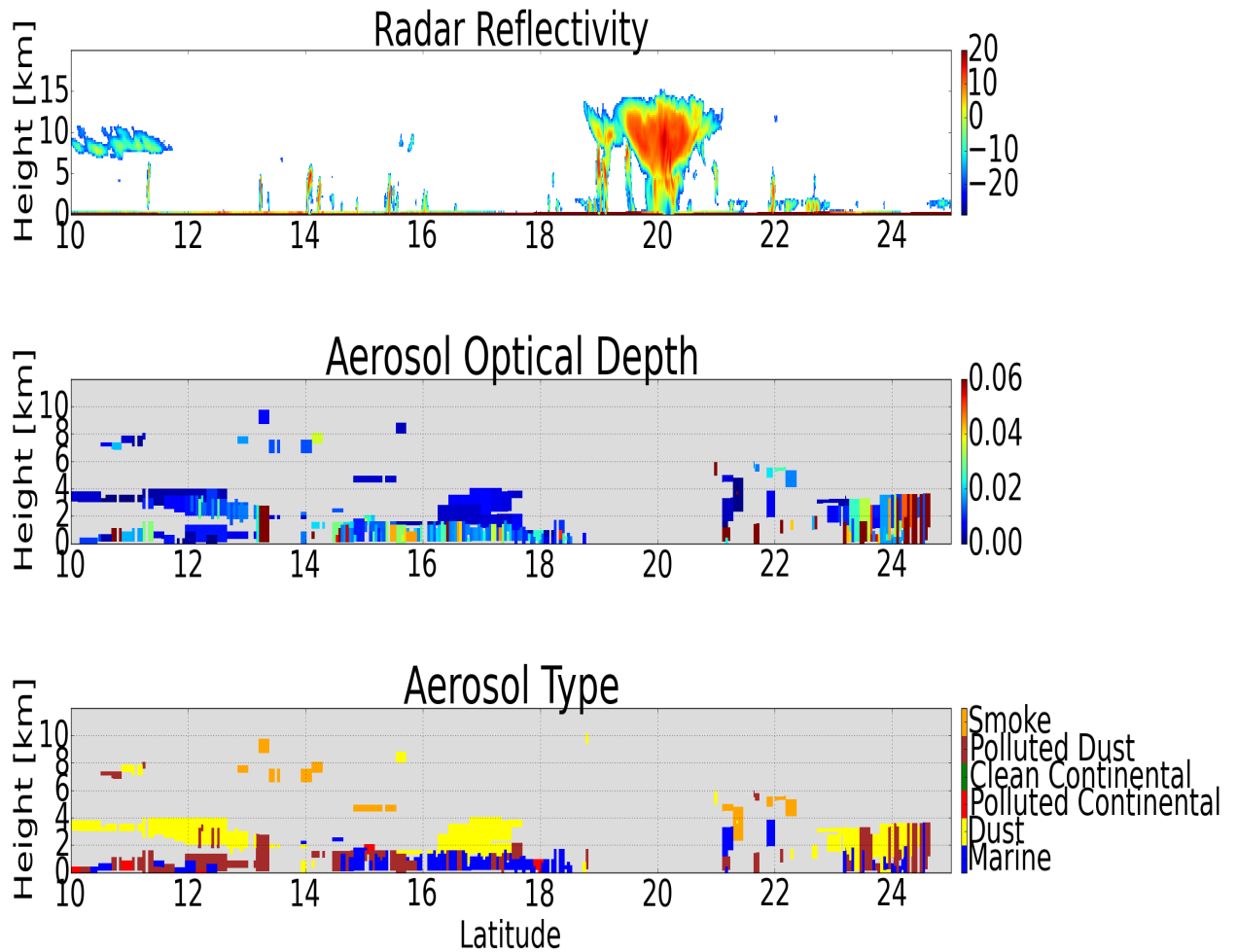
FIGURE 2.2: CloudSat reflectivity and CALIPSO aerosol optical depth and aerosol type from a segment of the A-Train orbit.

for evaluating the complete profile of clouds and aerosols.

CloudSat carries a, nadir-viewing, high power pulse radar termed the Cloud Profiling Radar (CPR). The CPR is the first-ever millimeter wave radar launched into space and measures the power backscatter from clouds as a function of distance from the radar. The instrument operates at 94.05 gigahertz (GHz) with -30 decibel (dBz) sensitivity. A high sensitivity performance of the radar is necessary as clouds are very weak scatterers. The radar uses 3.3-

microsecond (μs) monochromatic pulses allowing for a 500-meter (m) vertical range resolution between the surface and 30km. Measurements are averaged in .32-second (s) time intervals with a horizontal resolution of 1.8km along track and 1.4km across track, and a vertical resolution of 240m that provides nearly 1800 independent CPR measurements (Im et al., 2005). The top panel of Figure ?? illustrates the reflectivity profile for a segment of the full CloudSat orbit from 10°N to 25°N.

Used in tandem with CloudSat, CALIPSO carries three nadir- viewing instruments, which include two passive instruments, the Wide Field Camera (WFC) and the Imaging Infrared Radiometer (IIR), and an active lidar termed Cloud-Aerosol Lidar with Orthogonal Polarization (CALIOP). The WFC operates during daytime for cloud properties and has a spatial resolution of 125m with a 61km swath that covers the 620 nanometer (nm) and 670nm spectral region. The IIR operates at a 1km resolution over a 64km swath and uses radiances at 8.65μm, 10.6μm and 12.05μm (Winker et al., 2003). CALIOP is the primary instrument on CALIPSO and provides high-resolution vertical profiles of aerosols and clouds, particularly for thin layers. CALIOP is designed to acquire vertical profiles of two orthogonal polarization components with attenuated backscatters by clouds and aerosols at a visible wavelength of 532nm and a total backscatter laser signal at an infrared wavelength of 1064nm. The 532nm backscatter signal has a vertical and horizontal resolution of 30m and 333m below 8.2km and 60m and 1000m between 8.2km and 20.2km, respectively (Liu et al., 2012). CALIOP level 1b source data has a physical separation of 335m between each footprint and is collocated with the CloudSat radar footprint based on the same resolution and location, allowing for the

powerful three dimensional structure of clouds and aerosols that is provided when the CPR from CloudSat and the lidar from CALIPSO are used in conjunction (Liu et al., 2012).

CloudSat and CALIPSO both supply various level-2b products that contain derived geophysical variables from level 1b observations to analyze cloud and aerosol interactions with each other, as well as with the climate system. The primary level-1b CloudSat product is the calibrated radar reflectivity profiles, from which 2B-CLDCLASS, 2B-CWC-RO, 2B-FLXHR, 2B-GEOPROF, 2B-TAU, 2B-CLDCLASS-LIDAR, 2V-CWC-RVOD,2B-FLXHR-LIDAR and 2B-GEOPROF-LIDAR are derived (Stephens et al., 2002). Of particular interest to the present work is the CloudSat precipitation occurrence dataset, 2C-PRECIP-COLUMN. The algorithm is used in order to validate the convective algorithm that was created using PATMOS-x data. This CloudSat precipitation algorithm determines the likelihood and intensity of surface precipitation over open ocean between the atmospheric layers of 750 and 1000m by using radar reflectivity data near the earth's surface and an estimate of path integrated attenuation from surface reflection characteristics (Smalley et al., 2014). The precipitation rates and precipitation classification as convective, stratiform or shallow based on rain top height is provided from estimates of liquid water content, height of liquid precipitation top and freezing level (L'Ecuyer et al., 2009).

Cloud layers and heights are determined by the combined CloudSat and CALIPSO level-2 Geoprof Lidar product, (2b-GEOPROF-LIDAR), which also use the Moderate Resolution Imaging Spectroradiometer (MODIS) based level 2b cloud optical depth product (2b-TAU)

for the optical depth and mean effective radius of single layer clouds that are undetected by CloudSat.

The aerosol information used in this analysis is provided by the CALIPSO lidar backscatter retrievals, and the location and optical depth of aerosols are collected from the 5km aerosol layer product. For this analysis, CALIPSO information collocated to CloudSat is used to determine the aerosol base and top heights, optical depth at 532nm and aerosol type. Aerosol type is identified using the integrated attenuated backscatter measurements and volume depolarization ratio measurements, as well as surface type and layer height (Vaughan et al., 2009). The bottom two panels in Figure **??** represent the aerosol optical depth and aerosol type from the CALIPSO lidar retrievals for the corresponding CloudSat reflectivity scene. The CALIPSO aerosol models use a cluster analysis from the Aerosol Robotic Network (AERONET) dataset to categorize six aerosol types: Clean Continental, Dust, Marine, Polluted Continental, Polluted Dust and Smoke. These aerosol types are classified based on physical and optical properties, and an aerosol extinction to backscatter ratio (aerosol-lidar ratio) is derived for each type to compare with actual aerosol observation measurements (Omar et al., 2009). The dust aerosols of primary interest in this study are detected using the CALIPSO dust model, which uses the irregular shapes of dust particles to determine the aerosol-lidar ratios through a discrete dipole approximation (DDA) technique. Polluted dust is classified as dust having mixed with biomass burning smoke or urban pollution, which is most common in areas that are prevalent sources of both aerosol types such as West Africa and Asia. An aerosol-lidar ratio of 40 steradians (sr) at 532nm is allocated for dust, with polluted dust defined at 65 sr

(Omar et al., 2009). The 2b-FLXHR-LIDAR algorithm is essential for evaluating vertically resolved cloud precipitation and aerosol properties.

CALIOP is advantageous for distinguishing the difference between aerosols and clouds, uncertainties arise when determining the CALIPSO aerosol optical depth as well as the classification of aerosol type (Burton et al., 2010). Thick aerosol layers such as dust storms and biomass burning plumes may be misclassified as clouds due to the attenuation of CALIOP signals, resulting in an aerosol layer that is incorrectly identified. Aerosols with low aerosol optical depths, particularly when clouds are present, may also be misclassified as a cloud layer (Winker et al., 2009). Uncertainty in the aerosol- lidar detection ratio leads to a misclassification of aerosol type, which further results in an increase in fractional ambiguity as the aerosol optical depth increases. The Cloud-Aerosol Discrimination (CAD) score can be used in order to determine the confidence in detecting a cloud. These uncertainties must be recognized as thin dust layers may cause difficulty when lofted to upper levels of the troposphere (Yu et al., 2010).

2.3   PATMOS-x

To place the cloud and aerosol snapshots from CloudSat and CALIPSO into the context of the evolution and intensity of convection, PATMOS-x cloud products from the Geostationary Operational Environmental Satellite (GOES) East and Meteosat Second Generation (MSG) datasets are used. Data from two separate geostationary satellites cover the full spatial extent of the tropical Atlantic Ocean in our region of interest from 0°N to 35°N and 10°W to 80°W.

The GOES East data is used to cover the region from 80°W to 40°W, while the Meteosat satellites to extend coverage to the West Coast of Africa.

PATMOS-x is a satellite based climate data record generated by the National Oceanic and Atmospheric Administration (NOAA) and more recently the European Organisation for the Exploitation of Meteorological Satellites (EUMETSAT) Meteorological Operational satellite programme (MetOp) satellites (Heidinger et al., 2012). This dataset focuses on retrieving cloud and aerosol information from the five-channel, $.63\mu$m, 11μm, 1.6μm, 3.75μm, and 12μm, calibrated Advanced Very High Resolution Radiometer (AVHRR) observations and selected ancillary data that have been on board NOAA satellite instruments since 1978 Heidinger et al. (2014), Sun et al. (2015). NOAA's AVHRR provides valuable data for detecting clouds on a global scale at a spatial resolution of 1.1km at nadir over a 2500km swath.

PATMOS-x employs a level-2b file format that is composed of sampled pixels, allowing for the conversion of observations of brightness temperatures into radiances (Heidinger et al., 2014). The product types used for this study include the infrared cloud properties product from Algorithm Working Group (AWG) Cloud Height Algorithm (ACHA). ACHA is an optimal estimation approach that derives the cloud top height, cloud top temperature, 11μm cloud emissivity and an $11/12\mu$m -microphysical index from the 8.5μm, 11μm and 12μm observations (Walther et al., 2013). ACHA runs in advance of the Daytime Cloud Optical and Microphysical Properties Algorithm (DCOMP), which supports the solar reflectance cloud properties product. DCOMP generates estimates of cloud optical thickness, cloud effective

radius and ice/water path during daylight conditions. The retrieval is based on simultaneous measurements of a visible channel with conservative scattering and a shortwave infrared weakly absorbing channel, which is based on previous work done by (**?**). DCOMP was developed in order to apply the algorithm to a wide variety of sensors to generate cloud climate records that are useful to the community. The PATMOS-x, ACHA and DCOMP algorithms all include uncertainty estimates that should be taken into account, but do not affect this research in any significant manner as the limitations are confined to cloud optical depth estimation over snow and cloud detection in polar regions (Walther and Heidinger, 2012).

PATMOS-x data have been evaluated using a naive bayesian cloud detection scheme that was derived from CALIPSO. Clouds are detected by using a naive Bayesian cloud mask algorithm that is collocated with the polar orbiting CALIPSO data and uses Global Area Coverage (GAC) data to process PATMOS-x. This algorithm finds the AVHRR pixel closest to each 1km CALIPSO cloud layer pixel and then employs a nearest-neighbor approach combined with a polynomial fit to provide initial estimates of the collocated pixels for an entire GAC orbit (Heidinger et al., 2012). The GAC pixel data is then sampled to create a .1° x .1° product by using the GAC pixel closest in distance to the grid (Sun et al., 2015). This evaluation has shown to provide probability of detection metrics of around 90%over ocean and has indicated that PATMOS-x is in much closer agreement with existing global cloud detection datasets (Heidinger et al., 2012).

2.3.1 GOES East

GOES East is part of a collection of four GOES satellites that is located at 75°W and 0°N. The satellite is able to supply images from a small sector to the full extent of Earth's disk in five different channels (Beyer et al., 2004). The Imager and the Sounder are the two main instruments on the GOES satellite, which provide information on infrared and visible energy and vertical atmospheric profile information (Clark, 1983). The satellite utilizes cloud properties that are generated using the AVHRR PATMOS-x algorithms and derived products. The GOES based AVHRR PATMOS-x product suite focuses on atmospheric products that include cloud and aerosol information and extends to 40°N.

2.3.2 Meteosat Second Generation

The MSG geostationary satellites are incorporated into this analysis to extend the boundary of the GOES East satellite window to the western coast of Africa. MSG is a collection of three identical satellites, Meteosat-8, Meteosat-9 and Meteosat-10, each having an expected lifetime of seven years, where a standby satellite is in orbit after the launch of the previous satellite. Meteosat-8 and Meteosat-9 data is used for the extension of spatial coverage and were launched in August 2002 and December 2005, respectively. As an improvement to the previous Meteosat satellites, MSG supplies significantly enhanced services and products with 12 spectral channels, in addition to a spatial resolution of 3km at nadir (Schmetz et al., 2002a). Cloud properties and products are also generated from Meteosat using the AVHRR PATMOS-x algorithms, similar to GOES East. Figure **??** portrays the cloud top temperature retrieval from Meteosat from the same scene as the CloudSat reflectivity and CALIPSO
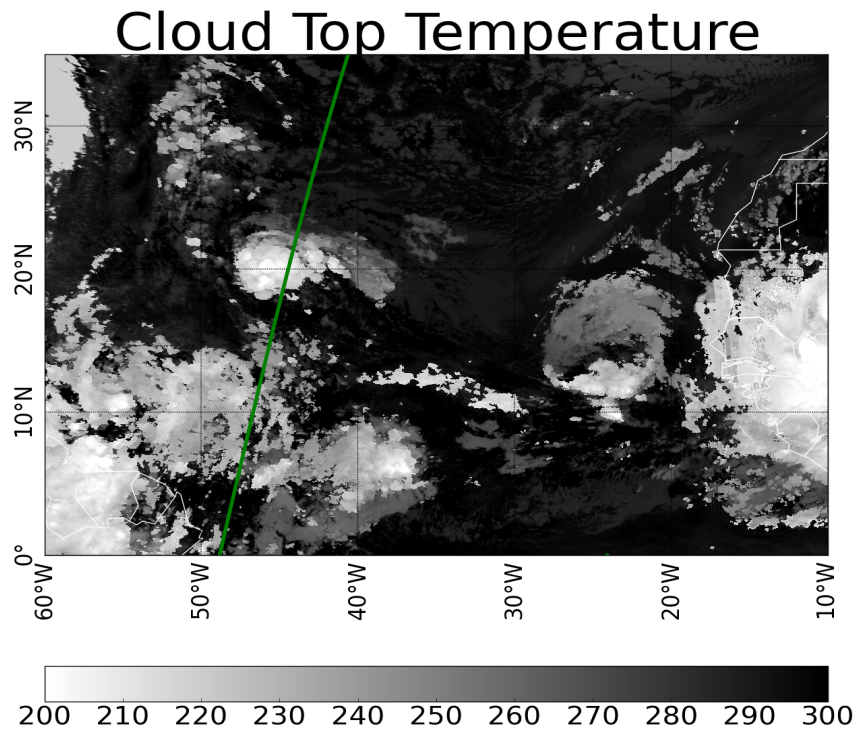
FIGURE 2.3: PATMOS-x Cloud Top Temperature from Meteosat for the same scene as Figure **??** and Figure **??**.

aerosol vertical profiles in Figures **??** and **??**. The quality control for all MSG products is greatly improved from previous Meteosat data, with solar channel calibration aimed at 5 % accuracy (Schmetz et al., 2002b) and an onboard blackbody calibration better than 1K for thermal channels (Pili, 2000). GOES East, Meteosat-8 and Meteosat-9 data products provide exceptional geostationary data for retrievals of convective processes and cloud microphysical processes for the investigation of mineral dust transport and redistribution.

Chapter 3

Methods

3.1   Introduction

While previous studies have assessed how the dust layer affects convection in the tropical Atlantic Ocean, this study investigates the role of convection on the dust layer using polar orbiting satellites for dust aerosol optical depth retrievals. A novel aspect of this approach is that it adds a time component to the polar orbiting dataset in order to track and monitor convection in a quickly changing atmosphere. Due to the infrequent, 16 day repeat cycle from the A-Train satellite constellation, PATMOS-x cloud product datasets must be collocated with the A-Train data to identify and track the evolution of convective storms in the region of study. These storms have significant impacts on the dust budget across the tropical Atlantic Ocean, as well as the redistribution of the dust once the convective storms pass through an area for both short and long time scales. To establish the total deposition of dust across the

tropical Atlantic Ocean, a budget analysis was performed to understand the dust layer and concentration of dust. To establish the component of this deposition owing to convection, datasets were collocated to identify convective storms. A full composite analysis on the dust layer around convection was then completed.

3.2 Budget Analysis

The amount of dust originating from the Saharan desert and sweeping across the tropical Atlantic Ocean can be quantified using the CALIPSO aerosol optical depth product. Following Kaufman et al. (2005), aerosol optical depth is converted to mass flux by using relationships between dust mass and optical thickness, to the dust size distributions that were obtained from a combination of several field experiments, AERONET measurements and model data. The mass column concentration for Saharan Dust can be estimated as:

$$M/T_{dust} = 2.7 +/- 0.4 g/m^2 \tag{3.1}$$

This ratio was also used by Koren et al. (2006) to calculate the amount of dust transported over large distances, as well as by Haywood et al., (2003) to present physical and optical properties of Saharan dust during the Saharan Dust Experiment (SHADE). For this research, the 2b-FLXHR-LIDAR-AUX product was used to capture the vertical distribution of aerosol optical depth from CloudSat and CALIPSO over thirteen, five degree longitude bands from 15°W-80°W and .25° latitude bands from 0°N to 35°N across the tropical Atlantic Ocean, as shown in Figure ??. The total mass of dust was then calculated over each latitude and longitude section for four years of data by multiplying the aerosol optical depth by the grid
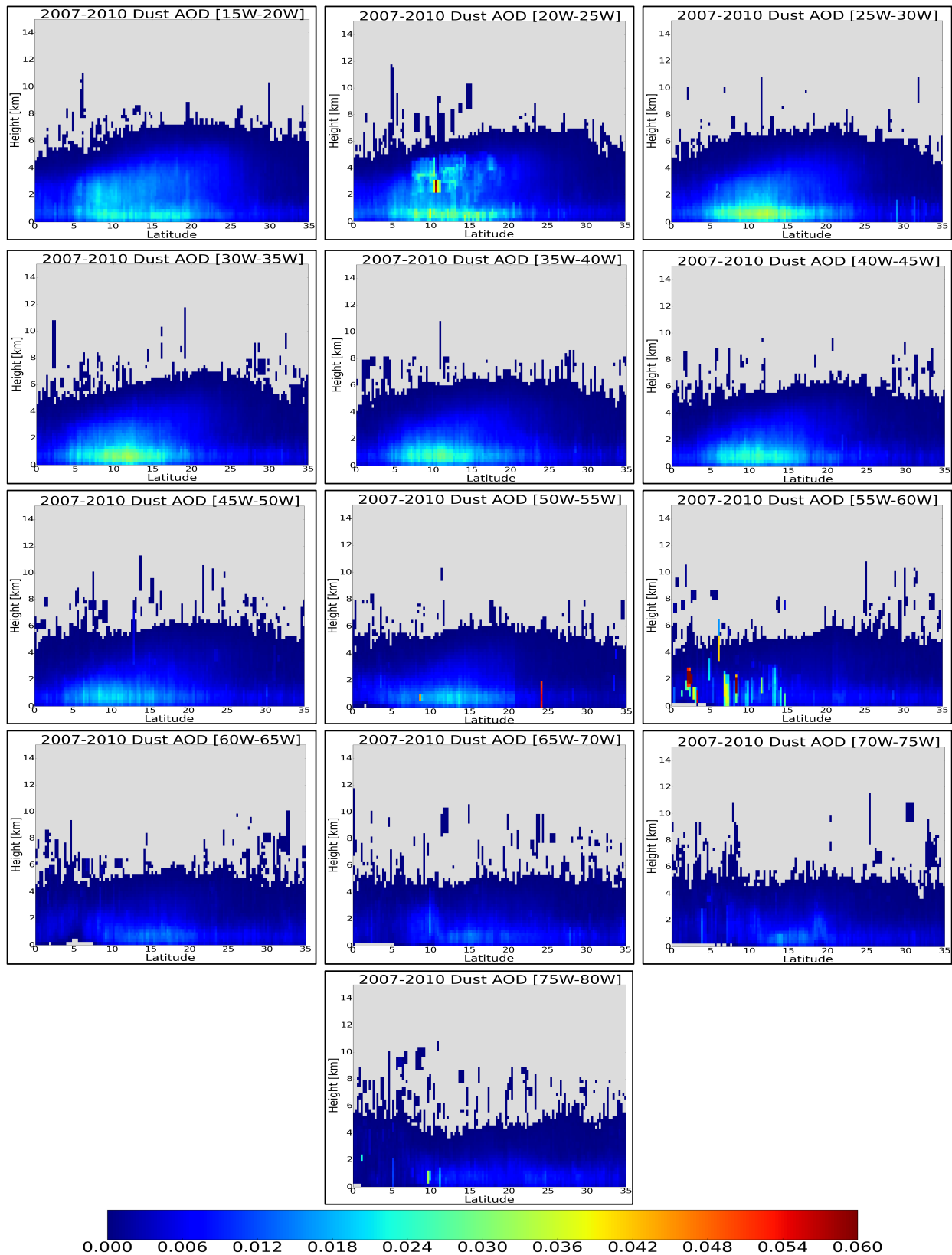
FIGURE 3.1: Vertical distribution of dust aerosol optical depth over each of the 13 longitude bands for .25° latitude bins for 2007-2010.
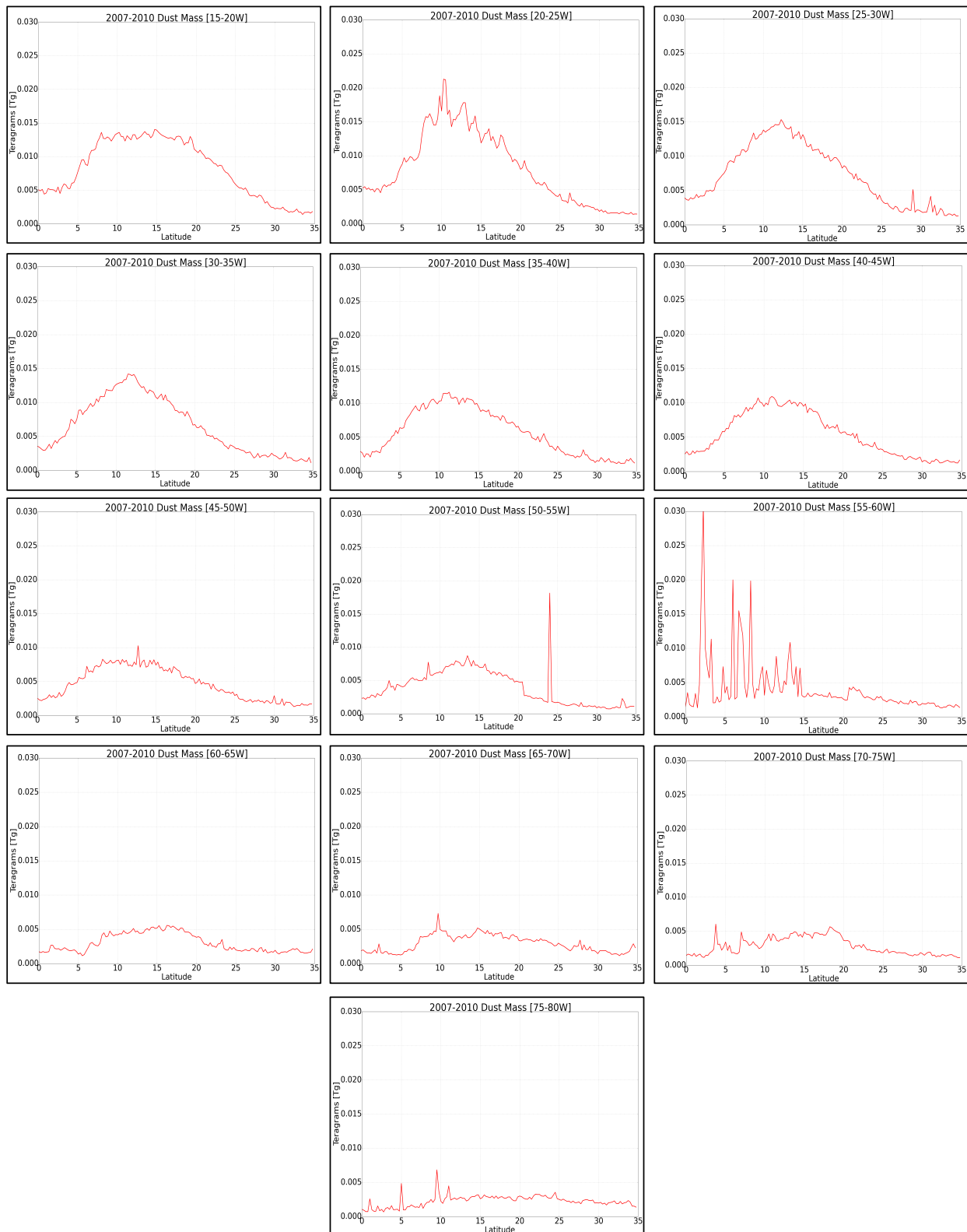
FIGURE 3.2: Total mass of dust in teragrams over each of the 13 longitude bands across the tropical Atlantic Ocean for 2007-2010.
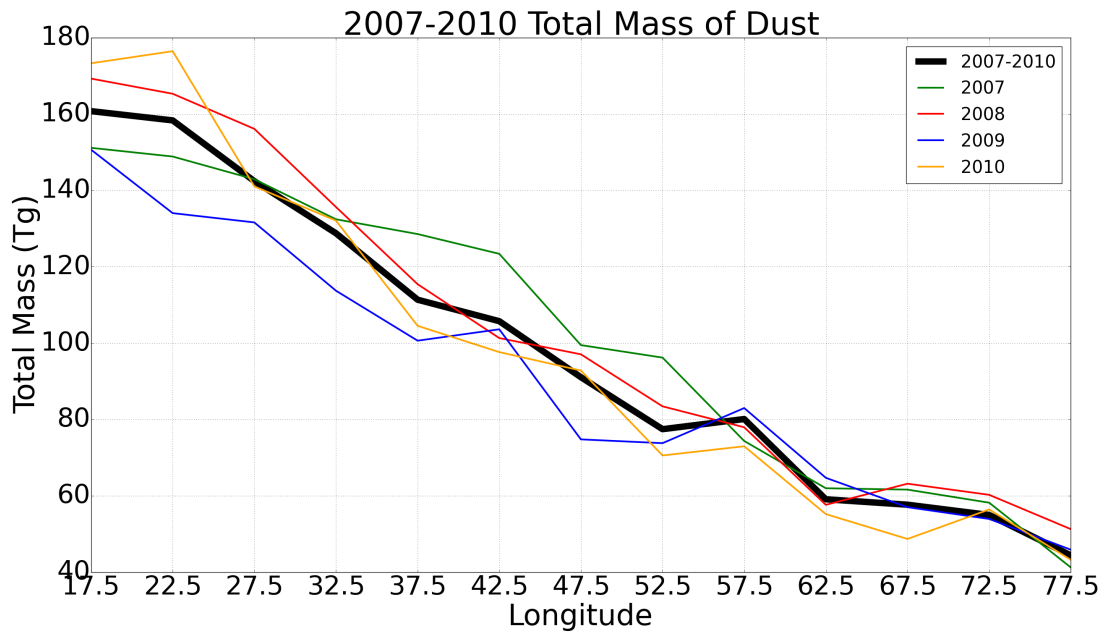
FIGURE 3.3: Total mass of dust in teragrams over each of the 13 longitude bands across the tropical Atlantic Ocean for 2007-2010. Each longitude represents the center of a five degree longitude band.

area, yielding the results shown in Figure **??**. Both images show a greater amount of dust closest to the source region, with the 15°W-20°W longitude band exceeding 0.85Tg of dust and the maximum aerosol optical depth reaching over .06 and extending through 8km in height in the 20°W-25°W band. As distance increases from the source region, the total mass and aerosol optical depths over all latitudes decrease as well, as can be seen in Figure **??**, which portrays the decline in the total mass of dust for all thirteen longitude bands and one latitude band as the dust layer moves west across the tropical Atlantic Ocean.

In addition, the amount of dust that was deposited into the ocean can be calculated between each longitude cross section. Since the source is the Sahara and the dust is advocated westward by the winds, the difference between what goes in to the eastern edge of a longitude box and
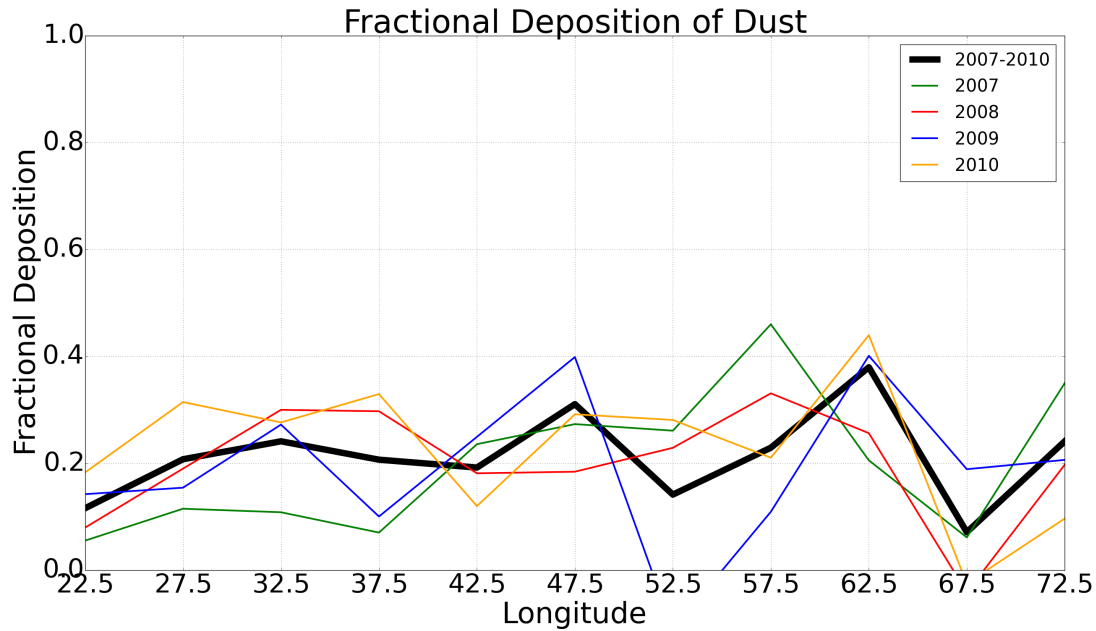
FIGURE 3.4: Fractional deposition of dust between each longitude band for 2007-2010, with each longitude representing the center of a five degree longitude band).

what goes out of the western edge must be deposited into the ocean. Figure **??** shows the fractional deposition of dust across the Atlantic Ocean between 15°W-80°W and 0°N to 35°N for 2007-2010. The graph indicates a relatively constant fraction of dust deposited in any given longitude band across the tropical Atlantic Ocean. Dust budget analyses for two individual, convective case studies, Tropical Storm Debby and Hurricane Helene, will be discussed in Chapter 4.

3.3   Collocating Datasets

To provide a more direct measure of the time-evolution of the aerosol field, the A-Train data were collocated with time-resolved cloud information from PATMOS-x data to allow for a continuous analysis of convection for determining the changes in vertical structure of dust

aerosol distribution before and after convection has passed through the region of study.
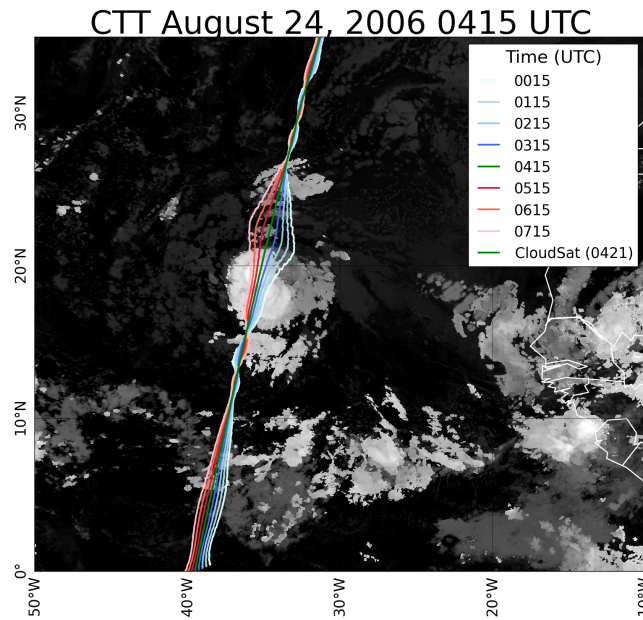
FIGURE 3.5: PATMOS-x cloud top temperature at 0415UTC with the CloudSat and CALIPSO overpass shown in green at 0421UTC. Each additional line represents the advection of the overpass due to wind values from MERRA-AUX for time before and after the overpass.

PATMOS-x cloud products from the closest time to the A-Train overpass, were matched to each CloudSat pixel using a nearest neighbor approach to establish a time-series of cloud properties associated with aerosol layer for each latitude and longitude pair along the CloudSat track in the tropical Atlantic Ocean (0°N-35°N and 10°W-80°W). Cloud products were then added from additional observation times before and after the CloudSat overpass to provide insights into the time-evolution of the cloud field around the overpass. Modern Era Retrospective- Analysis (MERRA)-AUX data was used to account for the advection of the dust layer time before and after the A-Train overpass to retrieve the cloud product information along the advected CloudSat track. Figure **??** shows the movement of winds around Tropical

Footprint Size (FS)	Area	Number of Pixels
1	616 (729) km^2	81 (5)
2	1601 (1773) km^2	197 (13)
3	3573 (3393) km^2	377 (29)
4	6037 (5517) km^2	613 (49)
5	9980 (10161) km^2	1517 (81)
6	13922 (13653) km^2	1129 (113)

TABLE 3.1: List of area footprint sizes and number of pixels in each footprint for GOES-East data (Meteosat).

Storm Debby for times before and after the CloudSat and CALIPSO overpass at 0421UTC. The lines for each time step are consistent with the movement of the storm, where times before the A-Train overpass are pushed westward as the Tropical Storm rotates counter-clockwise. Time steps for the collocated datasets for both Tropical Storm Debby and Hurricane Helene are shown in Figures ?? and ??, respectively, and provide a twelve-hour time step of the cloud top temperature retrievals, along with the MERRA winds. The CloudSat and CALIPSO overpass closest in time to the cloud top temperature retrieval is indicated with a white line, and the red line represents the wind advection from the MERRA-AUX dataset to show the movement of the winds around the storms. These two figures show how this procedure can allow for the air mass sampled by CloudSat and CALIPSO to be tracked for up to 12 hours prior to and after the overpass to determine if and when it may have interacted with convection.

Footprint Size (FS)	Average CTT (K)
1	240.5K
2	239.6K
3	241.6K
4	242.8K
5	243.6K
6	246.1K

TABLE 3.2: Average Cloud Top Temperature (CTT) for each footprint size in Figure ??
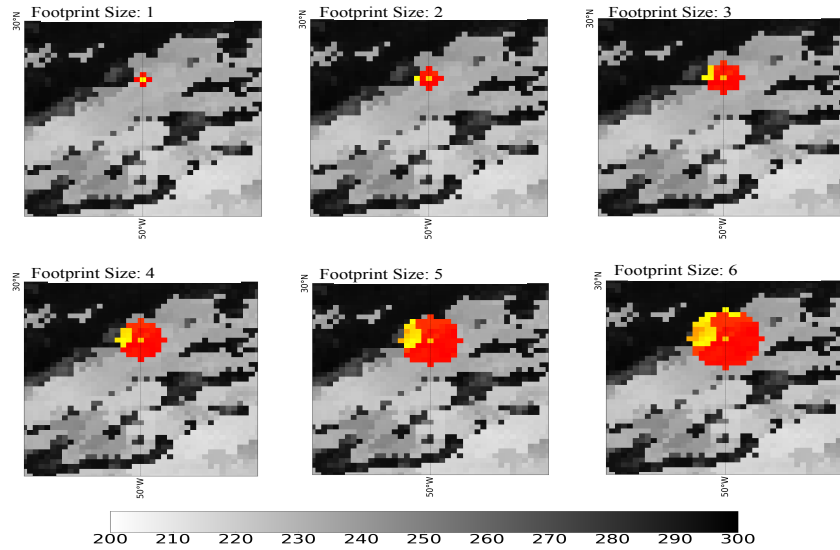
FIGURE 3.6: Spatial representation of cloud top temperature with each area footprint size for one scene in the tropical Atlantic Ocean.

3.4   Identifying Convection

Convective systems can be identified based on their areal extent as well as their cloud top temperatures (Mapes and Houze Jr, 1993). From the collocated dataset described in Section 3.3, convection was determined using thresholds on the area footprint rings for cloud top temperature and cloud optical depth. Once the single, collocated PATMOS-x pixel was established, the pixel was used as the central grid point to create an area footprint. Surrounding adjacent pixels were added to the footprint to increase the area. Table **??** shows the area and number of pixels for each footprint size (FS) for both the GOES-East and Meteosat data, while Figure **??** shows a sequence of the six area footprints around a single PATMOS-x pixel.

As more pixels are added and the footprint size increases, the average cloud top temperature for the footprint increases as well, indicated in Table **??**. Average cloud top temperatures
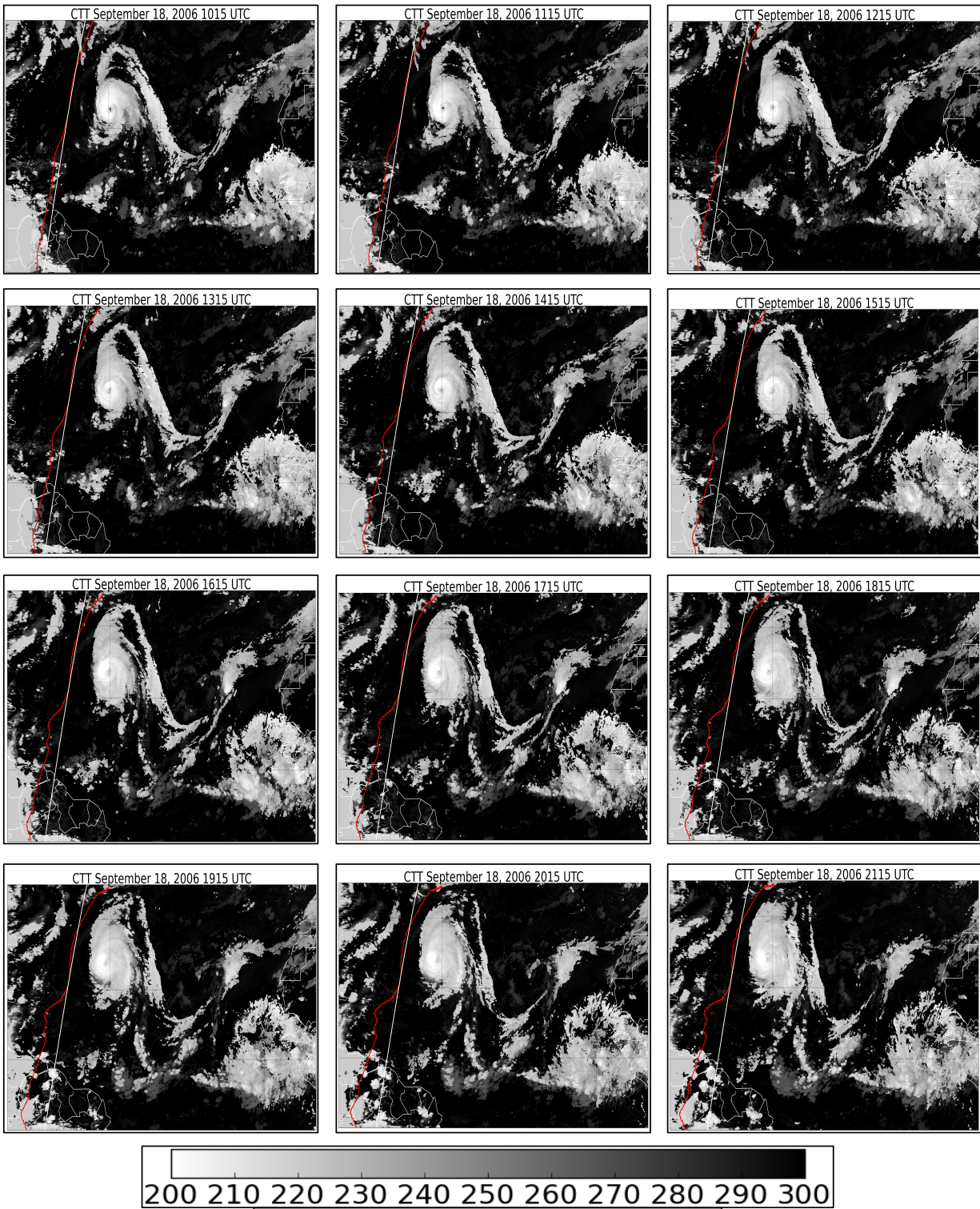
FIGURE 3.7: Meteosat cloud top temperature retrievals for twelve hours starting on September 18th, 2006 at 1015UTC and capturing the development of the storm until 2115UTC. The white colored line on each time step represents the actual CloudSat and CALIPSO overpass that occurred at 0545UTC. The red line indicates the wind advection from MERRA-AUX data after the A-Train overpass.
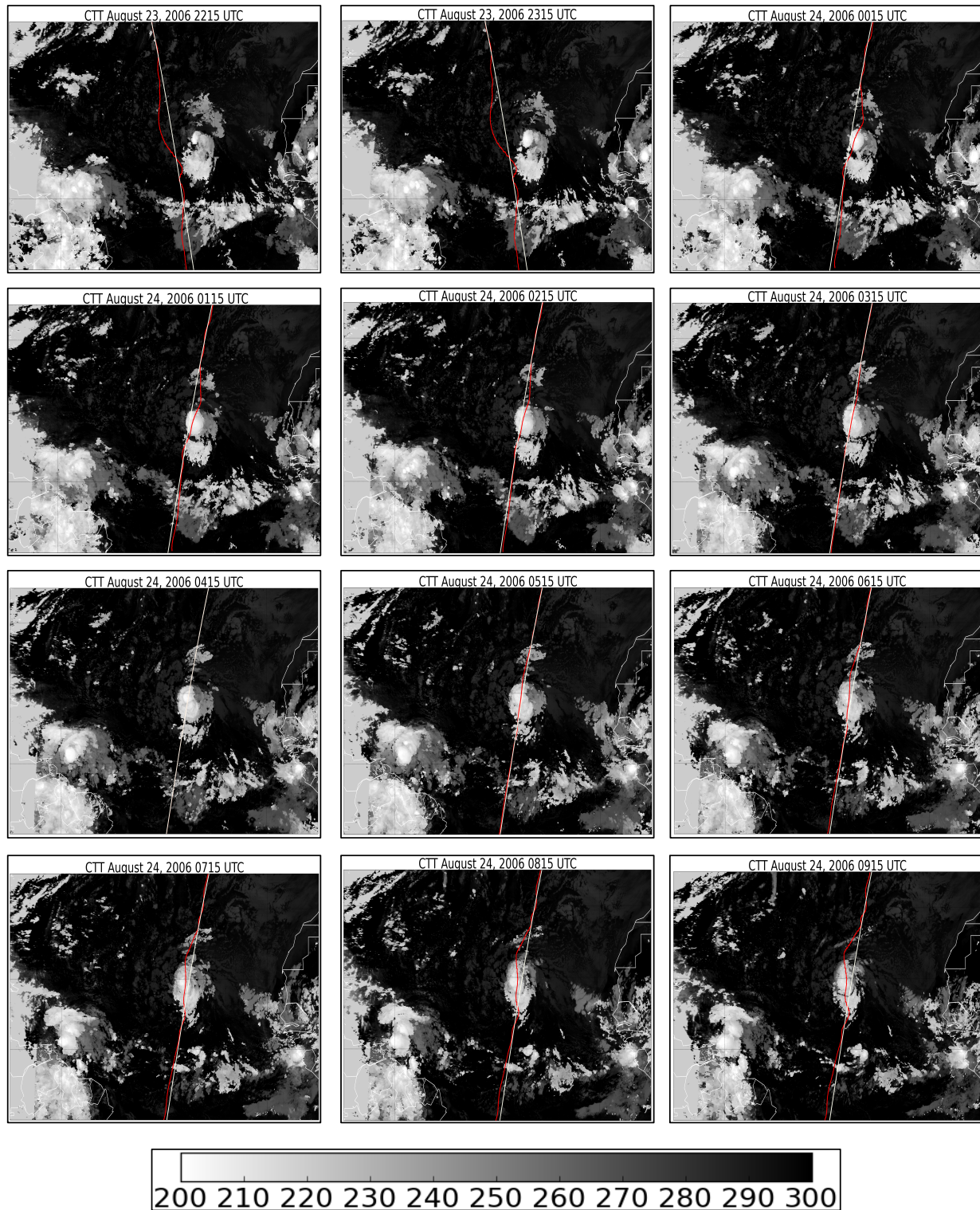
FIGURE 3.8: Similar to the Hurricane Helene time steps but for Tropical Storm Debby starting on August 23rd, 2006 at 2215UTC and capturing the development of the storm until 0915UTC. The white colored line on each time step represents the CloudSat and CALIPSO overpass at 0421UTC, with the red line indicating the wind advection from MERRA-AUX data before and after the A-Train overpass.

increase as the footprints increase because surface temperatures start to be averaged in as opposed to the cold cloud tops. The cloud top temperature, cloud top height and cloud optical depth from the PATMOS-x data were averaged over each area footprint for the collocated latitude and longitude points along the actual CloudSat overpass as well as the advected overpasses at times prior to and after the actual satellite observation time. Whenever cloud fraction in a given area footprint was less than .1, cloud temperatures are replaced with PATMOS-x surface temperatures. This information was stored in a datafile to then be able to use the cloud product information for each CloudSat granule to identify convection.

Three categories were defined including No Precipitation, Large Scale Convection and Small Scale Convection. No precipitation was flagged if the cloud top temperature footprint size-1 (FS-1) was greater than or equal to 285K. Figure **??** shows a flow chart of how the large and small scale convective flags were determined. Large scale precipitation scenes are first recognized if cloud optical depth FS-1 was greater than or equal to 5. This aids in distinguishing between small cirrus clouds, particularly anvil clouds that are associated with deep convective storms. Large scale and small scale convective storms were further distinguished from by requiring that the ratio between cloud top temperature FS-7 and cloud top temperature FS-1 for large scale convection and the ratio between cloud top temperature FS-4 and cloud top temperature FS-1 for small scale convection be greater than the ratio between cloud top temperature FS-2 and FS-1. This verified that the cloud top temperatures were decreasing from the center of the storm out towards the edges, with the larger storms including the larger area footprints. To identify large scale convection, if the average cloud top temperatures for

33

FIGURE 3.9: Schematic of Tropical Storm Debby on how mature convection is identified. As the area footprints increase in size, warmer cloud top temperatures are averaged together, therefore increasing the average cloud top temperature as footprint sizes increase.

all area footprints increased sequentially as the footprint increased area and cloud top temperature FS-1 had an average temperature less than or equal to 225K, mature convection was flagged. Small scale convection was flagged if the average cloud top temperatures for the first four area footprints increased as the area footprint increased and the cloud top temperature FS-1 was less than or equal to 240K. This threshold was used as a way of identifying convection because convective cores are the coldest portion of the storm, therefore as the footprint

33

FIGURE 3.9: Schematic of Tropical Storm Debby on how mature convection is identified. As the area footprints increase in size, warmer cloud top temperatures are averaged together, therefore increasing the average cloud top temperature as footprint sizes increase.

all area footprints increased sequentially as the footprint increased area and cloud top temperature FS-1 had an average temperature less than or equal to 225K, mature convection was flagged. Small scale convection was flagged if the average cloud top temperatures for the first four area footprints increased as the area footprint increased and the cloud top temperature FS-1 was less than or equal to 240K. This threshold was used as a way of identifying convection because convective cores are the coldest portion of the storm, therefore as the footprint

FIGURE 3.10: Flow chart representing how large scale convection and small scale convection was identified using PATMOS-x data.

increases over the top of the storm, warmer temperatures are averaged together. Several other temperature thresholds have been used for identifying convection such 215K, 219K and 235K in studies by (Arkin and Meisner, 1987, Arkin, 1979, Fu et al., 1990, Maddox, 1980). The thresholds implicated in this study were established using appropriate order of magnitude estimates from previous studies.

Figure **??** is an example of a convective storm with area footprints located on top of the storm, where the smallest cloud top temperature footprint has a lower average cloud top temperature and the largest footprint is warmer.

FIGURE 3.11: Radar reflectivity from CloudSat during Tropical Storm Debby with the mature convective flag from the PATMOS-x convective algorithm represented with red dots.

An example of the large scale convective flag is shown in Figure **??**. Red dots at the top of the image show where large scale convection was identified. In this case, the PATMOS-x convective algorithm identifies convection fairly well, with the exception of a few outliers. Since t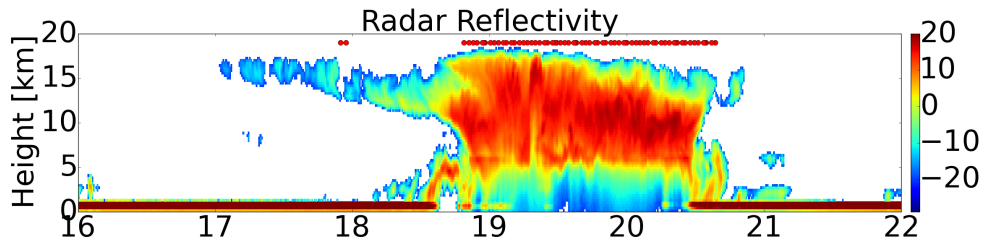his algorithm identifies convection only using cloud top temperature, cloud optical depth and area, the convective flags are not going to be exactly correct every time.

To test the algorithm, the PATMOS-x convective flag was then compared to the CloudSat and CALIPSO precipitation flag in order to gain a skill score of the newly created precipitation flag. The skill score was calculated by taking the number of times the new precipitation flag indicated mature convection or no precipitation at the same location where CloudSat indicated deep convection or no precipitation, and dividing the number by the total number of pairs of latitude and longitude points in the collocated PATMOS-x and CloudSat file. The skill score between the PATMOS-x and CloudSat convective algorithms for **??** is .94, indicating that the PATMOS-x convective algorithm is correct 94% of the time when compared to CloudSat. Once convection was defined, a composite analysis was performed to understand the effects of the identified convection on the dust layer, and determine how convection impacts the dust budget for individual storms as well as the full extent of the tropical Atlantic Ocean.
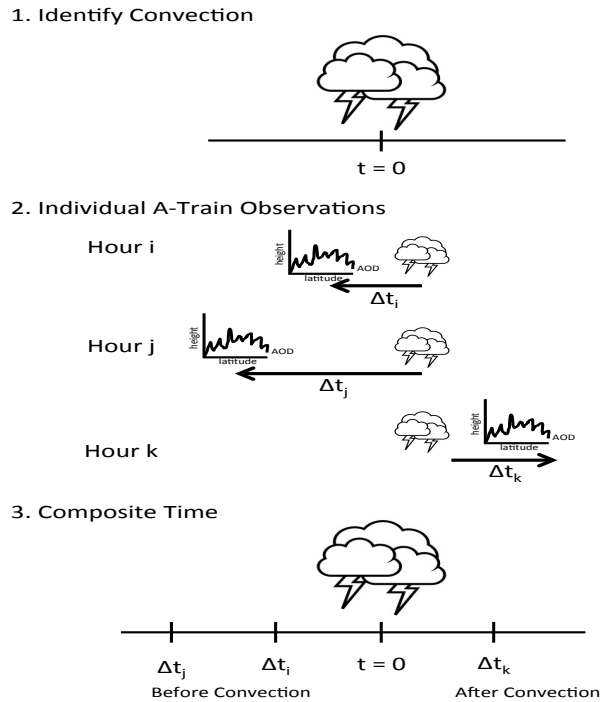
FIGURE 3.12: Schematic outlining the composite analysis. The first step is to identify convection using the PATMOS-x convective algorithm. CloudSat and CALIPSO aerosol optical depth observations in the same location are identified. Same time differences are then composited together around the identified storm.

3.5 Composite Analysis

With the identification of convection, a composite analysis was developed in a similar manner to Masunaga (2012). In his analysis, he composited a time series of temperature and humidity profiles from Aqua satellite observations before and after TRMM identified deep convection. These composites rendered results on the large-scale forcing and response of tropical and subtropical atmospheres to moist convection (Masunaga, 2012). For the purpose of this study, the aerosol layer was composited around convective events that were flagged by the PATMOS-x convective algorithm to show the effects of a typical convective storm system
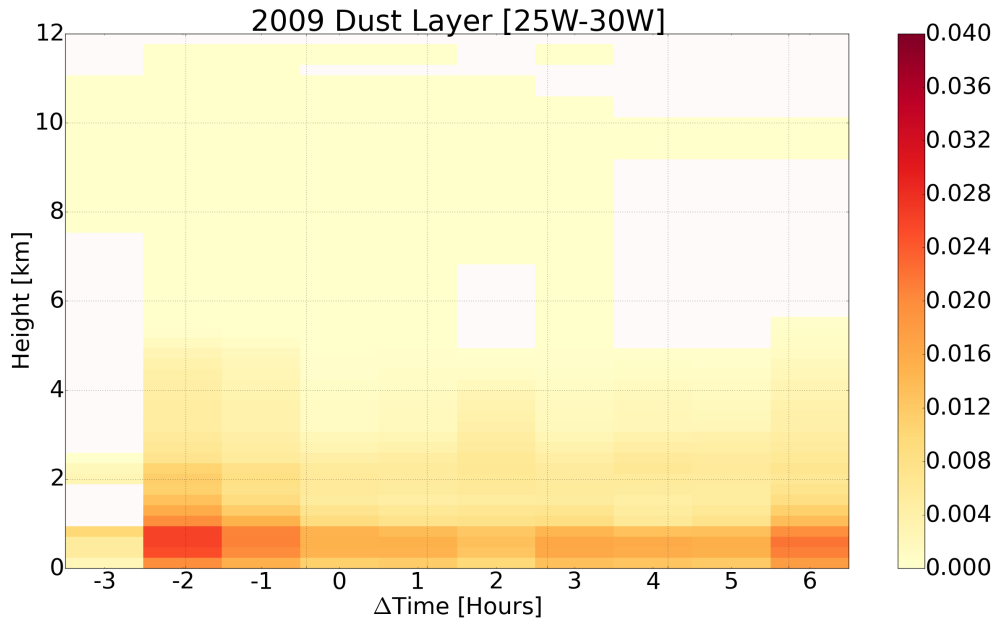
FIGURE 3.13: Average dust aerosol optical depth for 2009 over one longitude bands from 25°W to 30°W without the identification of convection.

lifecycle on the dust layer. When mature convection was flagged from the algorithm, the CloudSat and CALIPSO overpass at that location and closest time to the convection were sought out for the aerosol information. The cloud properties were taken from PATMOS-x for each hour, three hours before, six hours after and the time of the CloudSat overpass nearest convection in order to track the convective storm through time. The aerosol layer was then analyzed by finding all CloudSat and CALIPSO overpasses within the composited time period to determine how the convection impacted the aerosol layer. Aerosol information was averaged together for each time period for the location of convection and two latitude degrees on either side of the identified convection. A schematic of this compositing technique is shown in Figure ??, which was adapted from the technique by Masunaga (2012). Because the analysis was looking at the dust layer around convection and the lidar from CALIPSO

became fully attenuated when thick clouds were present, the aerosol data was interpolated to fill in gaps where convection was observed.

Once the composites were completed, the effect of no identified convection on the dust layer can be compared to areas that have identified convection. Figure **??** represents what the composited aerosol information looks like without identifying any convection and using the average dust layer for the same time period for one of the five degree longitude bands from 25°W to 30°W and a latitude region of 10°N to 30°N. Without identifying convection, the dust layer has a slightly lower aerosol optical depth as the dust is distributed around a larger area as opposed to right around the convective cell. In the absence of convection, there is not an obvious change in the dust layer with time. The composited aerosol optical depth data around identified convection can then be subtracted from the corresponding longitude bands in Figure **??** to determine the effect of mature convection on the average dust layer in 2009. Convective composites for all thirteen longitude cross sections as well as the differences between the average dust layers, were created to interpret the impacts of convection across the entire tropical Atlantic Ocean and are discussed in Chapter 5.

Chapter 4

Individual Storm Case Studies

Before looking at how convection effects the dust layer across the entire tropical Atlantic Ocean, two case studies that developed out of African Easterly Waves (AEWs) were examined to analyze the effects of individual, mature organized storms. AEWs are disturbances that originate over and near the African continent and are located in the low-level tropical easterlies. These disturbances are caused by temperature gradients between the hot, dry air from the Saharan Desert and the cooler air rising from the south. AEWs seldom develop into tropical storms and hurricanes, but in cases where they do, there is a significant impact on the dust layer (Zipser et al. (2009)). Two case studies are presented where one AEW developed into a Tropical Storm and a second AEW matured into a category three hurricane.

4.1   Tropical Storm Debby

Tropical Storm Debby, hereafter TS Debby, formed near the Cape Verde Islands from an AEW originating in an area southwest of the Arabian Peninsula, Asir Mountains and Ethiopian Highlands. TS Debby began formation on August 21, 2006 at 1800UTC around (10°N, 21°W) and became a tropical storm on August 23, 2006 at 0000UTC (Zhu et al., 2015). Cooler sea surface temperatures under the center of the storm promoted a shortened intensification time period, ultimately causing the dissipation of the tropical storm into a low-pressure disturbance (Zipser et al. (2009)). TS Debby was observed to interactive with the SAL and occurred during the NASA African Monsoon Multidisciplinary Activities (NAMMA) field experiment in 2006, which provided more information on the SAL and AEW formation around the Cape Verde Islands (Zipser et al. (2009)).

There were 32 A-Train overpasses during the lifetime of TS Debby, allowing for a full analysis of the dust distribution before, during and after the storm passed through the tropical Atlantic Ocean. The storm moved northwest through an area from 10°N to 25°N, and 20°W to 50°W. Figure ?? shows the cloud top temperature from PATMOS-x data on August 24, 2006 at 0415UTC, with the blue dashed line indicating the CloudSat and CALPSO overpass track before the storm moved through the area 24 hours before the overpass on August 23, 2006 at 0330UTC. The solid green and red dashed lines represent the overpass examined in this study for during and after the storm. The blue and red solid lines show the 6 hour increments of wind advection for up to 24 hours before and after the overpass to understand the movement of dust aerosols in the region. The yellow boxes indicate the section of the overpass where
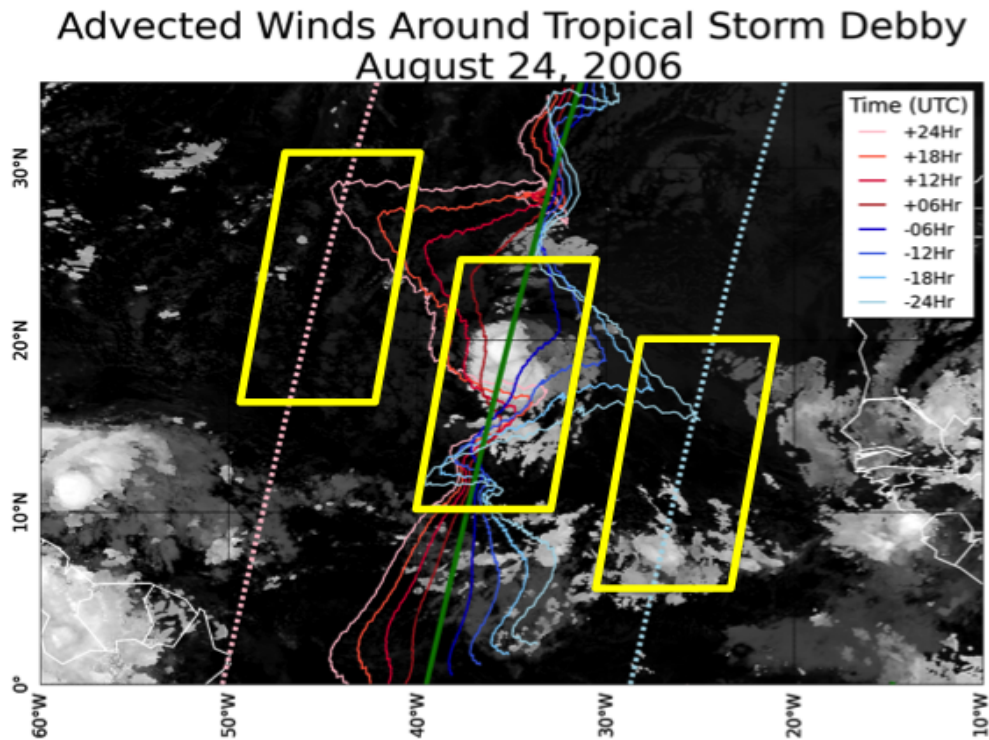
FIGURE 4.1: Cloud Top Temperature retrieval from Meteosat on August 24, 2006 at 0415UTC during the Tropical Storm Debby overpass with advected winds for 24 hours before and after overpass.

the storm moved through, corresponding to the region where the aerosol layer was analyzed. The reflectivity, aerosol optical depth and aerosol type from CloudSat and CALIPSO before the storm on August 23 are presented in Figure **??**. The aerosol optical depth had fairly high values, reaching just over 0.5 in the center of the dust layer, where the dust and polluted dust were mainly between 0km and 6km for latitudes between 12°N and 25°N. The dust layer was easily distinguishable just before 20°N, where it became elevated to about 2km, with a thin marine layer located beneath. The section between 17°N and 19°N indicates a clear scene because of the attenuation of the lidar from CALIPSO, even though there is most likely dust aerosols in that location.

FIGURE 4.2: Reflectivity, Aerosol Optical Depth and Aerosol Type between 5°N and 20°N on August 23, 2006 at 0330UTC before Tropical Storm Debby overpass.

Approximately 24 hours later, another CloudSat and CALIPSO overpass occurred on August 24, 2006 at 0421UTC directly over TS Debby, where the storm was located between 18°N and 21°N. The PATMOS-x cloud top temperature at 0415UTC is shown in Figure **??** with the CloudSat and CALIPSO overpass in green and advected winds for 24 hours before and after the overpass to show where the aerosols may be coming from and the direction in which they are moving towards. The tropical storm is fully developed at this point, with tight formation in the center of the Atlantic Ocean.

Figure **??** illustrates the reflectivity, aerosol optical depth and aerosol type for the A-Train overpass, where the aerosol optical depth is indicating a variety of lofted dust and polluted dust particles around the edges of the storm. These lofted aerosol particles may be due to the

FIGURE 4.3: Reflectivity, Aerosol Optical Depth and Aerosol Type between 10°N and 25°N during the TS Debby overpass. The PATMOS-x precipitation flag is located in the reflectivity image, with yellow indicating stratiform precipitation and red mature convection.

convective storm moving particles around with the motion of the storm or via wet deposition processes from the anvil of the storm. The particles that were lofted had very low aerosol optical depths, while the highest aerosol optical depths at the lower levels reached 0.48, which is slightly lower than the highest aerosol optical depth before the storm passage.

At 0500UTC on August 25th, 2006, CloudSat and CALIPSO observed a third overpass after TS Debby had passed, as seen in Figure ?? by the red dashed line. The aerosol optical depth in Figure ?? shows a dust layer slightly different compared to before the storm, where the dust layer that encompassed dust and polluted dust aerosols was slightly elevated above a thin marine layer between 2km and 5km. The aerosol layer after the storm passed through was slightly lower in height after the storm exited the region, as can be seen when comparing the mass concentration values in Figure ??. Panels a, b and c in Figure ?? show the mass
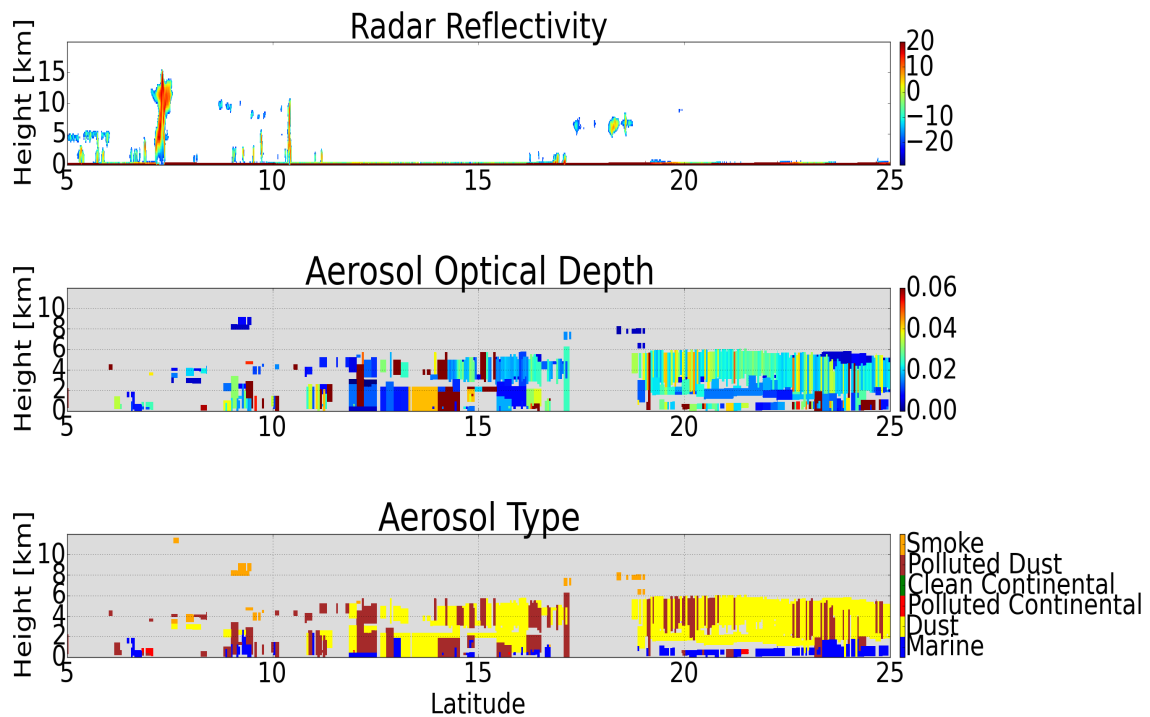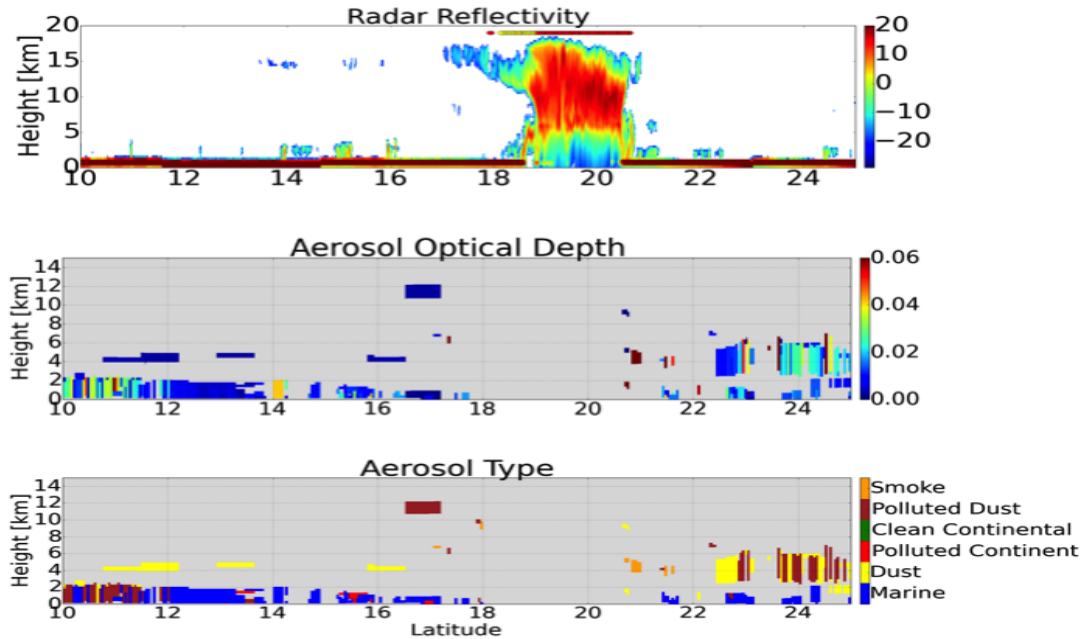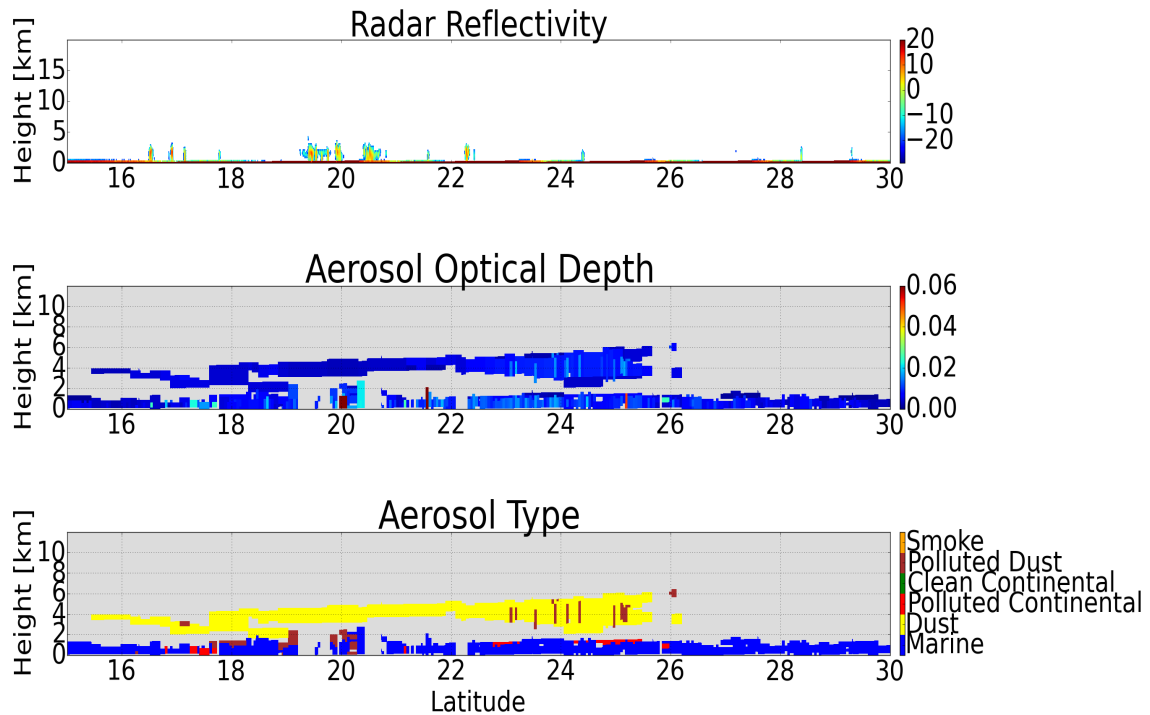
FIGURE 4.4: Reflectivity, Aerosol Optical Depth and Aerosol Type between 15°N and 30°N after the Tropical Storm Debby overpass.

concentration values for the individual overpasses before, during and after the tropical storm, where the lofted particles can be seen during the storm in Panel b, between 8km and 12km. Panel d, e and f illustrate the differences in mass concentrations between during and before, after and during and before and after the storm, with the scavenged mass concentration amounts on each Panel. Positive values in Panel d represent more dust during the storm overpass, while negative values portray more dust before the storm transitioned through the region. The positive values show how there are lofted aerosols, particularly between 6 and 8km and 10 and 12km during the overpass of Tropical Storm Debby. Panel e compares the mass concentration of dust after the storm to during the storm. This image shows more dust at lower levels after the storm compared to during, while lofted aerosols that were seen in
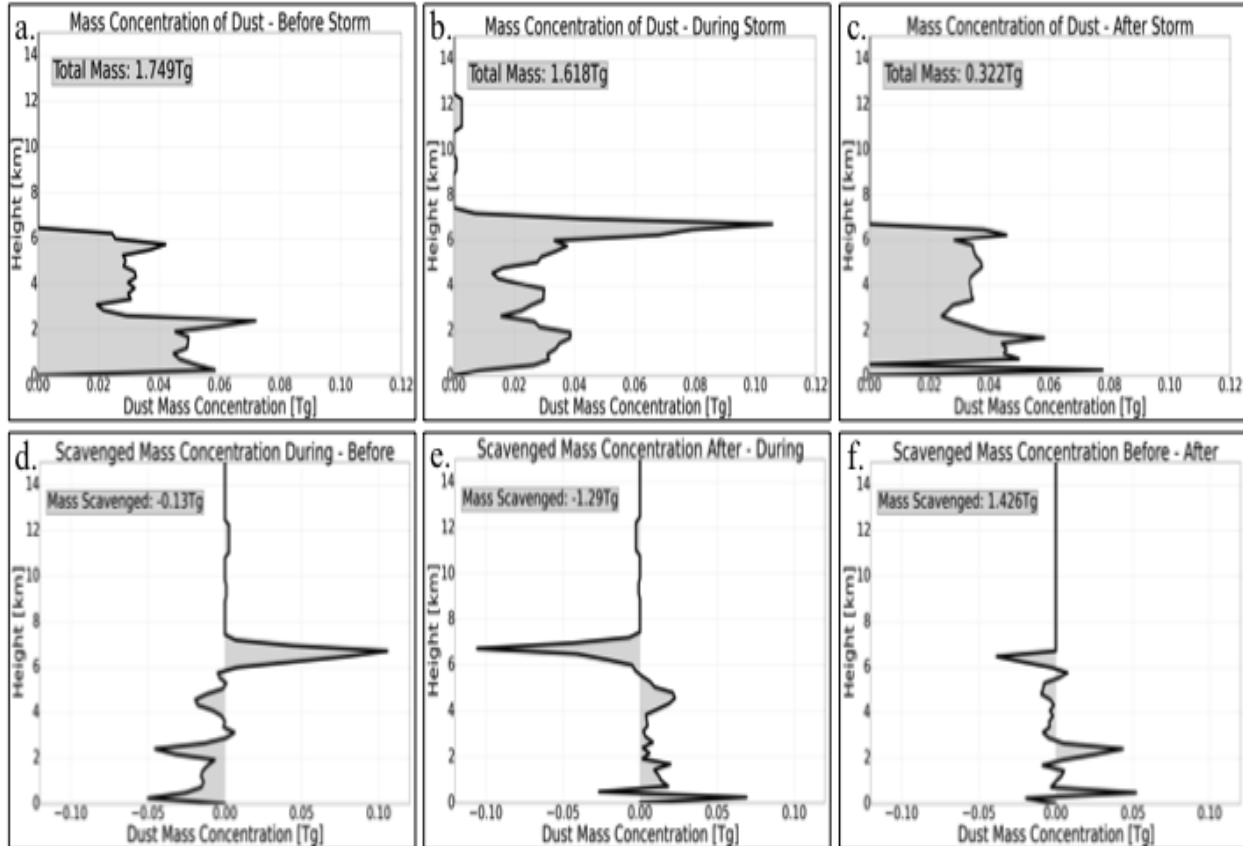
FIGURE 4.5: The amount of dust before, during, after and scavenged between before, during and after for Tropical Storm Debby.

the positive values in Panel d are still showing higher concentrations at their respective levels compared to before the storm. Looking at the difference in mass concentration of dust before and after the storm, 1.42Tg of dust was scavenged after the storm passed. Most of the mass concentration was located at lower levels before the storm, as shown in positive values, while aerosols were redistributed to between 3km and 7km after the storm overpass. Comparing the deposition rate before and after the storm, there is a significant difference where there is about .072Tg/hour of dust being deposited before the storm and .013Tg/hour deposited after the storm.

TS Debby was shallow and relatively small in area, having active but weak convection due to strong shear between the 5km and 8km level throughout its lifetime. According to Zipser et al. (2009), African dust may have been a major factor in the decreased intensity of TS Debby, because of the ingestion of the dust layer into the storm. The case study presented shows how the dust layer was disturbed during the storm overpass and then altered after the storm, relative to pre-storm conditions.

4.2   Hurricane Helene

In addition to Tropical Storm Debby, a second AEW developed into Hurricane Helene during the NAMMA field campaign. A strong tropical wave formed off of the coast of Africa in early September 2006, and by September 12th at 1200UTC, a Tropical Depression had emerged. Although the storm was slow to develop because of the enormous size of the depression, on September 13 the Tropical Depression turned into Tropical Storm Helene. As the storm moved over warm waters of the eastern Atlantic Ocean, the storm strengthened, although not significantly fast because of the ingestion of the dust layer. However, the storm began to intensify as shear weakened and the tropical storm developed into a hurricane on September 16th. Hurricane Helene peaked at a category three hurricane in the early hours of September 18th with winds reaching 120 miles per hour (mph) and a minimum pressure center of 962 millibar (mb). Once the motion of Hurricane Helene moved north, the strength of the hurricane downgraded to a category one hurricane and continued to weaken until September 24th when the hurricane dissipated into an extra tropical cyclone as it moved northeastward towards Ireland (Schwendike and Jones, (2010)).

Between September 12th and September 20th, 2006, there were 38 CloudSat and CALIPSO overpasses that went through 10°N to 35°N and 20°W to 55°W. Since Hurricane Helene had a prolonged lifetime, there were two favorable locations across the tropical Atlantic Ocean where CloudSat and CALIPSO overpasses were present before and after the passage of the storm. This gives the ability to provide a quantitative assessment of the changes in the dust layer as the convective storm transitions across the Atlantic Ocean through the above mentioned
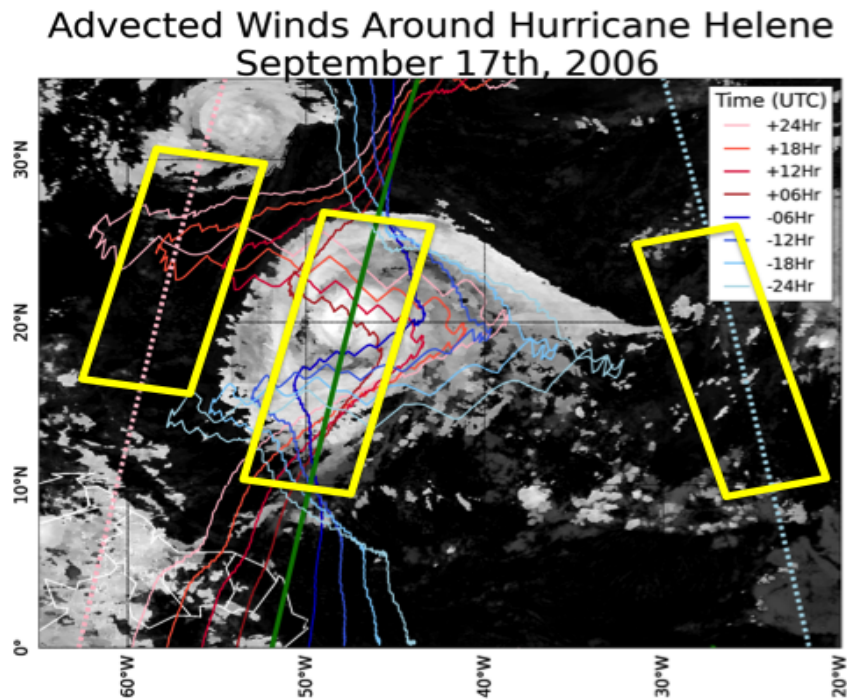
FIGURE 4.6: Cloud Top Temperature retrieval from Meteosat on September 17, 2006 with advected winds during the Hurricane Helene overpass.

region of interest. Figure **??** shows the PATMOS-x cloud top temperature on September 17th at 0505UTC, with the blue dashed line indicating a CloudSat and CALIPSO overpass 24 hours before the storm on August 16th at 1515UTC. The yellow box on the blue dashed line corresponds to the region where the reflectivity, aerosol optical depth and aerosol type for before the storm overpass are pictured in Figure **??**, with a defined dust layer between 10°N and 20°N.

The dust aerosols are located primarily between 0km and 4km, representing the center of the dust layer. The aerosol optical depths peak around .26 between 10°N and 21°N, again being consistent with the location and characteristics of the dust layer. Approximately 24 hours
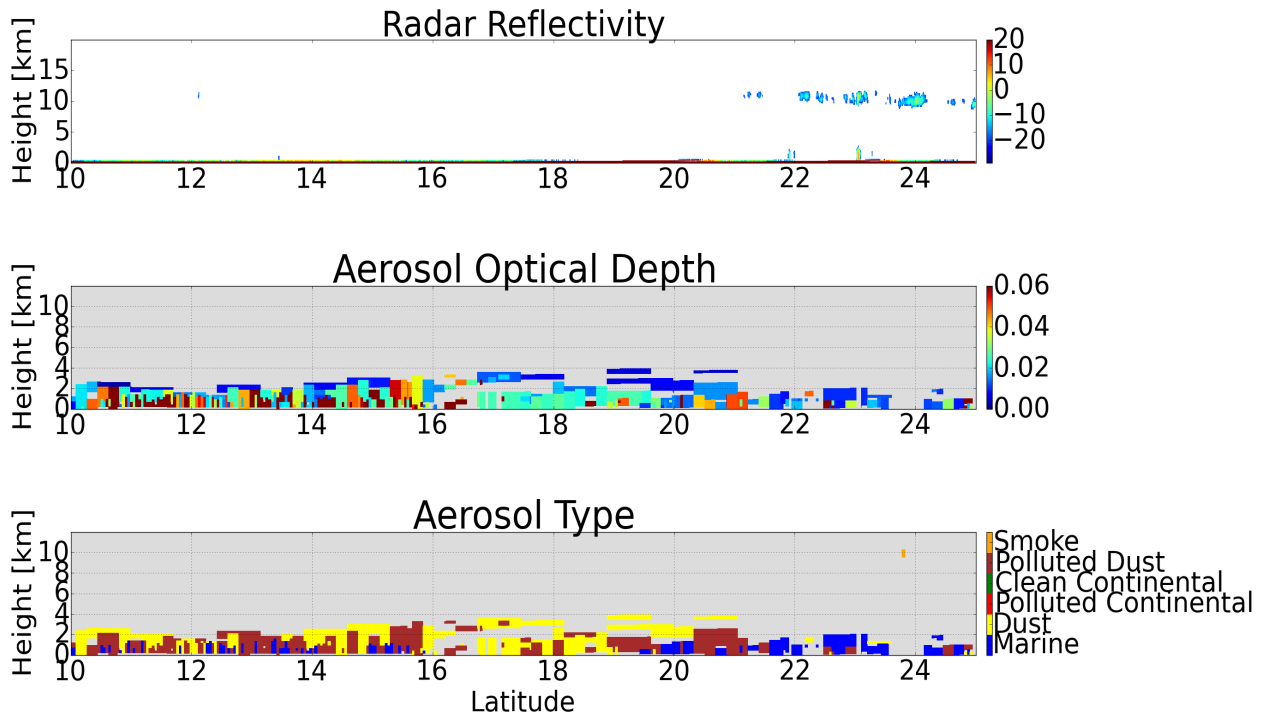
FIGURE 4.7: Reflectivity, Aerosol Optical Depth and Aerosol Type between 10°N and 25°N before the Hurricane Helene overpass. The PATMOS-x mature convection identification is indicated at the top of the reflectivity image in red circles.

later on September 17, 2006, there is a CloudSat and CALIPSO overpass during Hurricane Helene, as seen in Figure **??** in the green solid line. This image is the PATMOS-x cloud top temperature once again, with advected winds around the overpass for 24 hours before and after to show where dust aerosols may have originated from and where they may be transported to. This image shows the large spatial extent of Hurricane Helene as the system moves across the tropical Atlantic Ocean. Figure **??** shows the reflectivity, aerosol optical depth and aerosol type for the hurricane overpass, with a significant amount of lofted aerosol around the outer bands and anvil regions of the hurricane, which is very similar to what was seen in the Tropical Storm Debby case. Again, the lofted particles have very low aerosol optical depths, while the highest values are in the lower layers and reach about .74. The
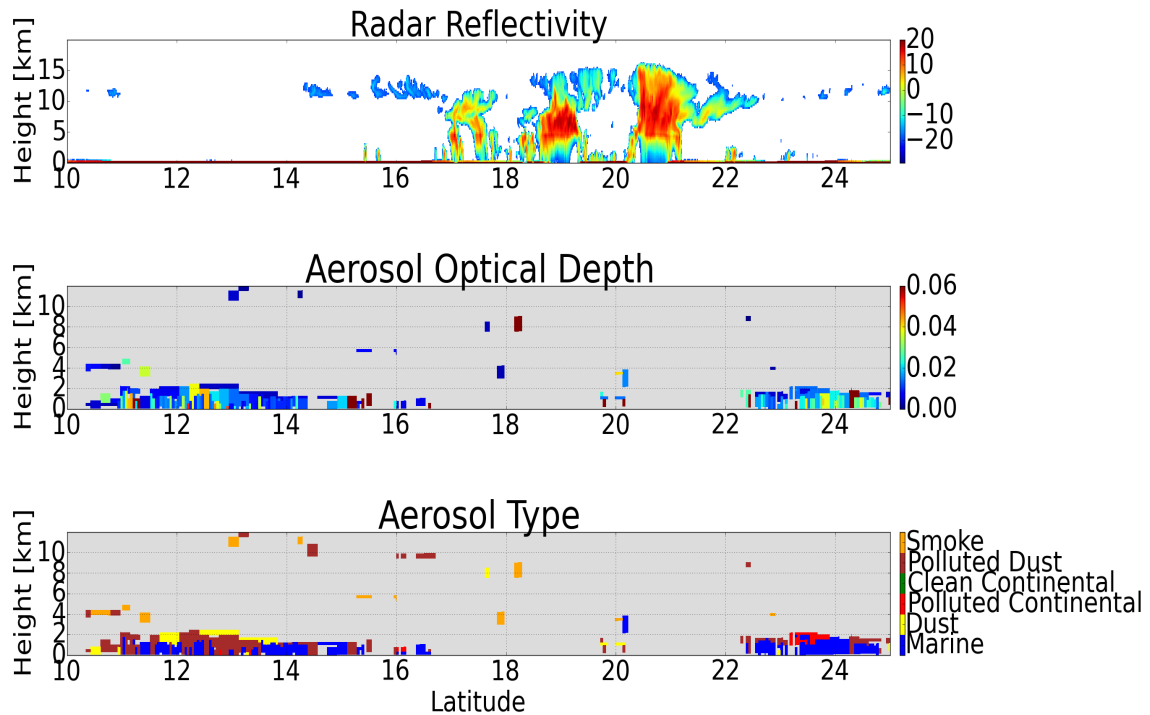
FIGURE 4.8: Reflectivity, Aerosol Optical Depth and Aerosol Type between 10°N and 25°N during the Hurricane Helene overpass.

aerosol optical depths during the overpass of the hurricane are slightly higher compared to the overpass before the storm, indicating potential wet or dry deposition or advected dust aerosols due to the storm.

The dust layer after Helene moved through this area is quite different compared to before the storm overpass. The red dashed line in Figure **??** represents the CloudSat and CALIPSO overpass approximately 24 hours after the storm on September 18th at 0545UTC. The aerosol optical depth illustrated in Figure **??** is slightly lower than before the storm, with maximum aerosol optical depths around 0.25, and the height of the aerosol layer about 2km lower after the storm overpass compared to before the storm overpass. When comparing the mass concentrations before, during and after the passage of the storm, Panels a, b and c in Figure **??**
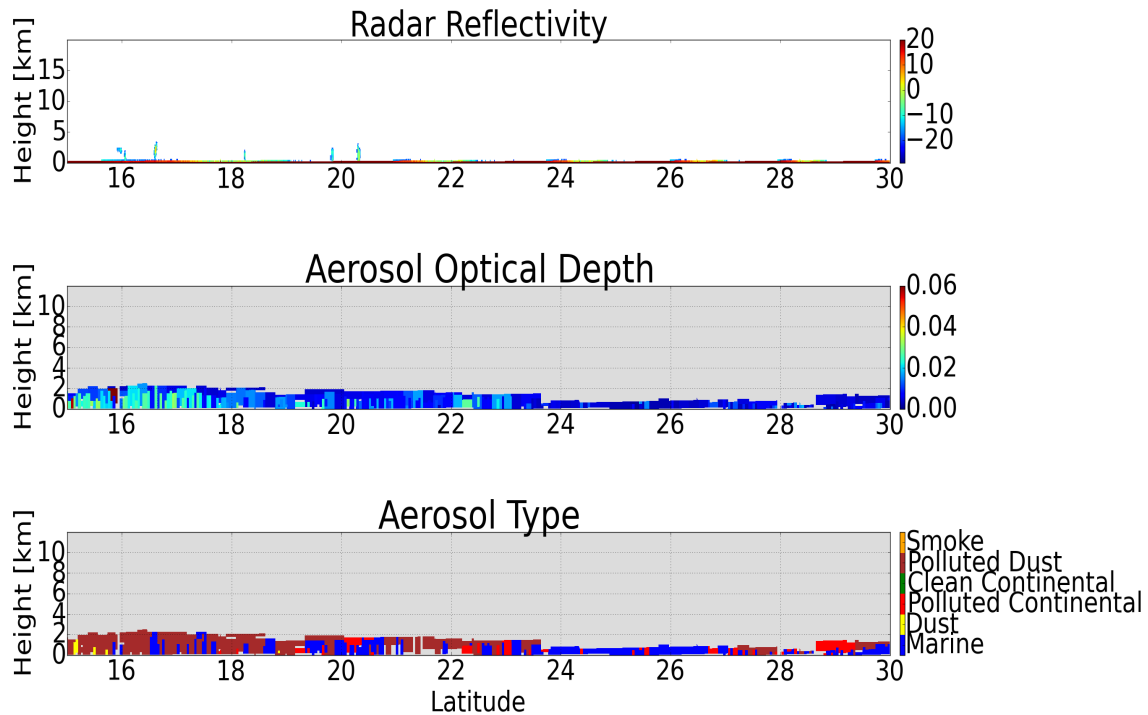
FIGURE 4.9: Reflectivity, Aerosol Optical Depth and Aerosol Type between 15°N and 30°N after the Hurricane Helene overpass.

show the concentrations for before, during and after the storm. Similar to TS Debby, Panels d, e and f indicate the differences between during and before, after and during and before and after the storm. The lofted aerosols during the storm can be seen in Panel b at 4km, 8km and 12km. Panels d and e also show there there are higher dust aerosol concentrations at these elevated layers during the storm compared to before and after the storm. The difference in mass concentration before and after Hurricane Helene is shown in Panel f, where positive values indicate where more dust was redistributed after the storm. There is a layer between 1km and 3km where dust aerosols were redistributed after the storm and had a higher mass concentration. About .45Tg of dust was scavenged after Helene passed through the region, where before the storm the deposition rate was approximately .031Tg/hour and after the
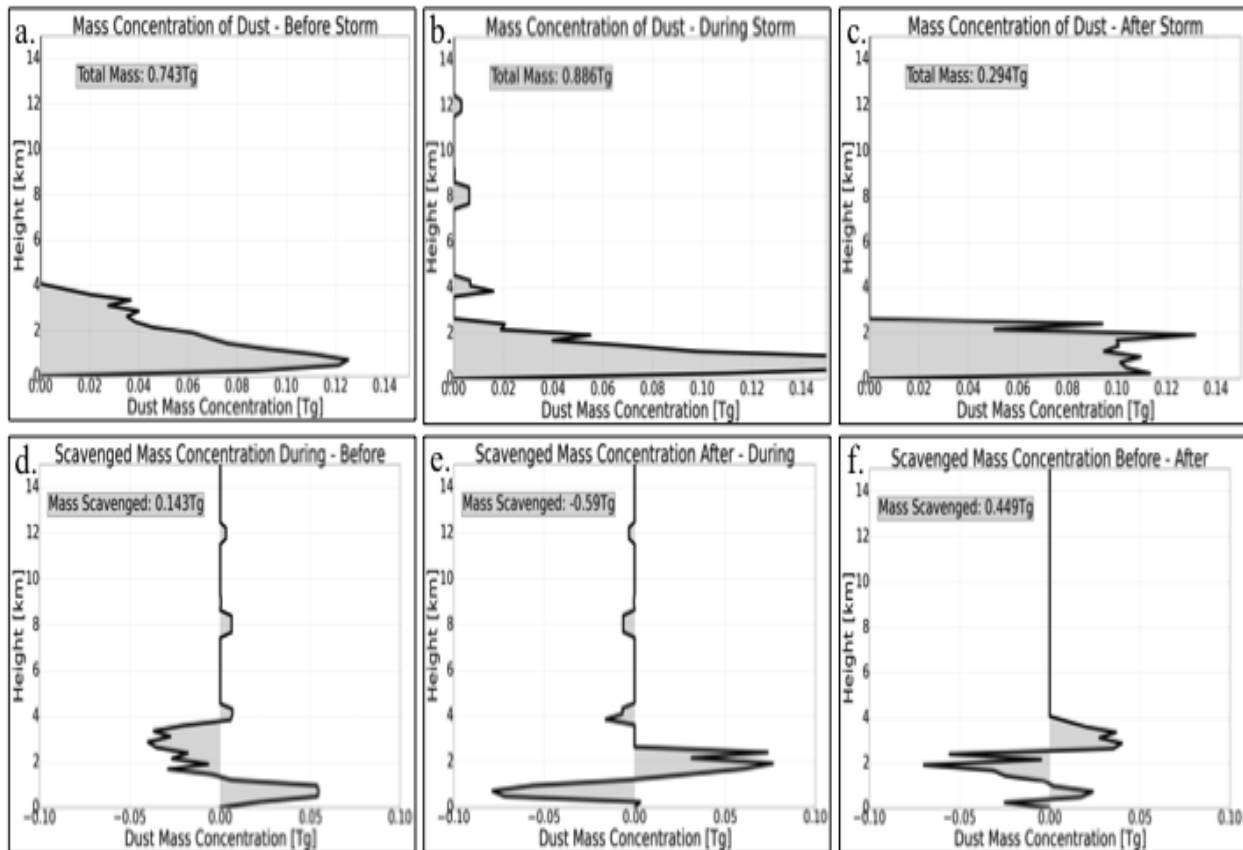
FIGURE 4.10: The amount of dust before, during, after and scavenged between before, during and after for Hurricane Helene.

storm the deposition rate was about .012Tg/hour. A very limited concentration is located right at the ocean surface where there was dust that had settled most likely due to wet or dry deposition.

4.3 Discussion

When comparing the two storms, there are similar qualities about the dust layer that occur once the storms move through a region. The two locations show slightly different results in

terms of the amount of dust in the area, but the location of the dust before and after each storm moves through the respective longitudes present similarities.

Tropical Storm Debby shows a redistribution of dust aerosols from a layer just above the surface and 2km in the atmosphere to just above 2km and 6km, while Hurricane Helene indicates dust that was redistributed to between 1km and 3km in the atmosphere. There was also a slight increase in the depth of the lower layer after the storm overpasses where dust from upper levels had transitioned to. Comparing TS Debby to Hurricane Helene, both storms that were formed out of AEWs present analogous results, where both dust layers are thicker and have higher aerosol optical depth values before a storm overpass compared to after a storm overpass and there were lofted aerosols during the overpass of the storm. These two storms are impressive examples of the effect convective events have on the transport and redistribution of the dust layer in the tropical Atlantic Ocean.

Chapter 5

Composite Analysis

The two cases presented in Chapter 4 provide strong evidence that large, organized tropical storm systems can exert a significant local influence on the distribution of SAL dust. To provide a more general estimate of the role of convection in redistributing dust across the Atlantic, the precipitation and convective fraction from the CloudSat precipitation dataset was compared against the net deposition of dust across the thirteen longitude bands previously defined in the tropical Atlantic Ocean. By comparing the effects of total precipitation fraction against the convective fraction to the net deposition of dust, we are able to identify the significance of convection on the dust layer. Figure 1.1 represents the CloudSat precipitation fraction on the left and the CloudSat convective fraction on the right compared to the net deposition of dust across the tropical Atlantic Ocean. The precipitation fraction on the left indicates an increase in total precipitation across the Atlantic, while the net deposition decreases. This inverse relationship provides evidence of having an increase in precipitation
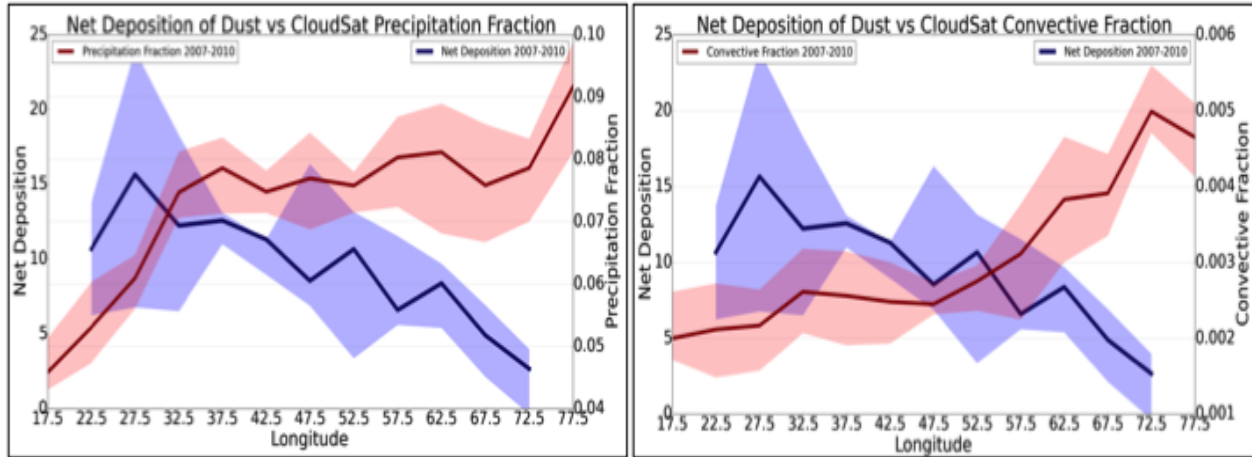
FIGURE 5.1: CloudSat Precipitation Fraction, left, and Convective Fraction, right, compared to the Net Deposition of Dust across the tropical Atlantic Ocean between 10°W-80°W.

effect the amount of dust that is in a certain longitude band. When looking explicitly at the convective fraction, the same relationship applies, where the net deposition decreases in regions where the convective fraction increases, yielding the investigation of the dust layer around convection.

As convection impacts the total net deposition across longitudes in the tropical Atlantic, the vertical redistribution of the dust layer is also of importance. The individual storms in Chapter 4 indicated lofted dust particles around the large convective storms, providing justification into an investigation of elevated dust layers in the atmosphere. Panel a in Figure 1.2 refers to the fraction of dust particles that have been elevated to layers greater than 6km in the atmosphere over the four year period. These particles have a distinct gap between the dust layer and the layer that is elevated, to ensure there is actual evidence of lofting instead of simply a deep dust layer. The majority of the lofted aerosol is located around regions above 30°N in the Atlantic Ocean, as well as a portion just east of South America. These
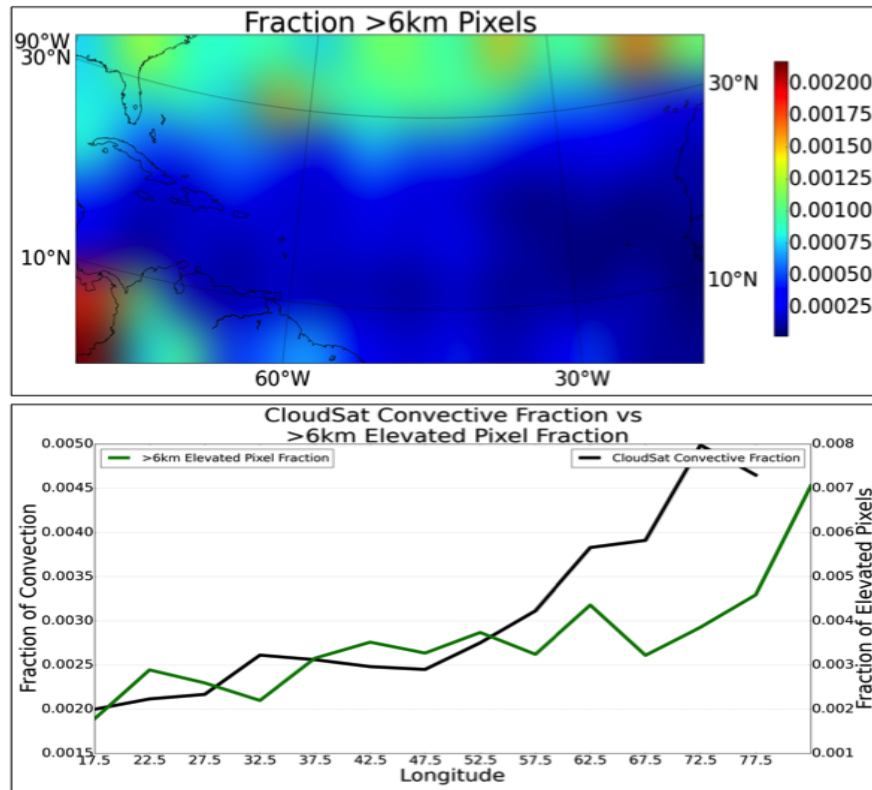
FIGURE 5.2: Fraction of elevated dust particles that were greater than 6km in the atmosphere and had a gap between the main dust layer and the elevated layer compared to the CloudSat convective fraction.

elevated pixels can then be compared to the convective fraction from CloudSat in Panel b of Figure 1.2, to observe if there is a correlation between the lofted dust aerosol and convection. As seen in the figure, there is a positive relationship between the fraction of lofted aerosol particles and the convective fraction from CloudSat. Moving across the ocean basin there is an increase in the convective events as well as increase in the amount of lofted dust aerosol above 6km. These figures provide the statistical basis for hypothesizing that convection is both redistributing and enhancing scavenging of the dust layer. To test this hypothesis and demonstrate causality, we need to explicitly examine the evolution of the dust layer in time as convection passes. Since that is not possible from individual satellite snapshots, we adopt

the compositing procedure.

5.1   Composites

A composite analysis was completed for 4 years of data between 2007 and 2010 to observe how convection impacts the dust layer for 7, ten degree longitude bands across the tropical Atlantic Ocean from 10°W to 80°W. The 7 longitude cross sections that are shown and discussed in this paper are represented in Figure 1.3. These figures show the composite temporal sequence of aerosol optical depth over −10 hours and +10 hours around convective occurrences for each longitude section and ± two degrees of latitude around each convective pixel for a region between 0°N and 35°N . The numbers at the top of each figure in brackets represent the number of pixels that were identified as convection for the composited hour.

Comparing the longitude cross sections for both day and night CloudSat and CALIPSO overpasses combined, there are general similarities between all cross sections. In the hours leading up to a convective event, the dust layer has a higher aerosol optical depth value and begins to increase in height, particularly between 1 and 8 hours before convection is identified. In all cross sections, there is a lower number of observations in the 4 hours before and 7 hours after convective identification due to the overpass time of CloudSat and CALIPSO in this region. The overpasses that cross at this time do not fully cross through the longitude box, therefore decreasing the number of observations. Once the convection occurs, the aerosol optical depth decreases in thickness for about 6 to 7 hours after convection occurs most likely due to deposition from the convection. The dust layer thickness then begins to rebuild around
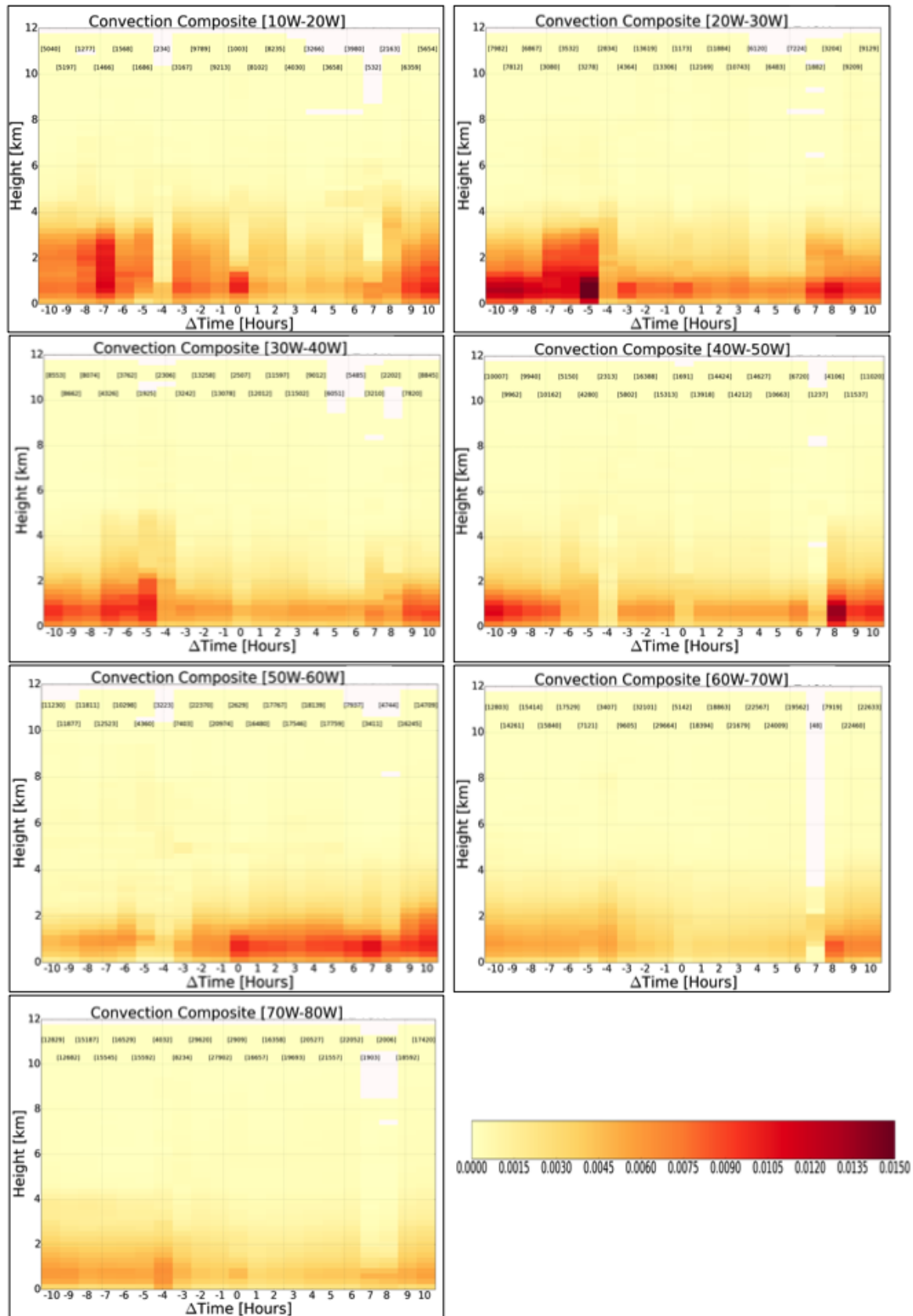
FIGURE 5.3: Composite observations of the vertical distribution of dust aerosol optical depth before, during and after from collocated CALIPSO, CloudSat and PATMOS-x data. Results for 10°W-80°W in ten degree increments are presented for ten hours before and after convective events.
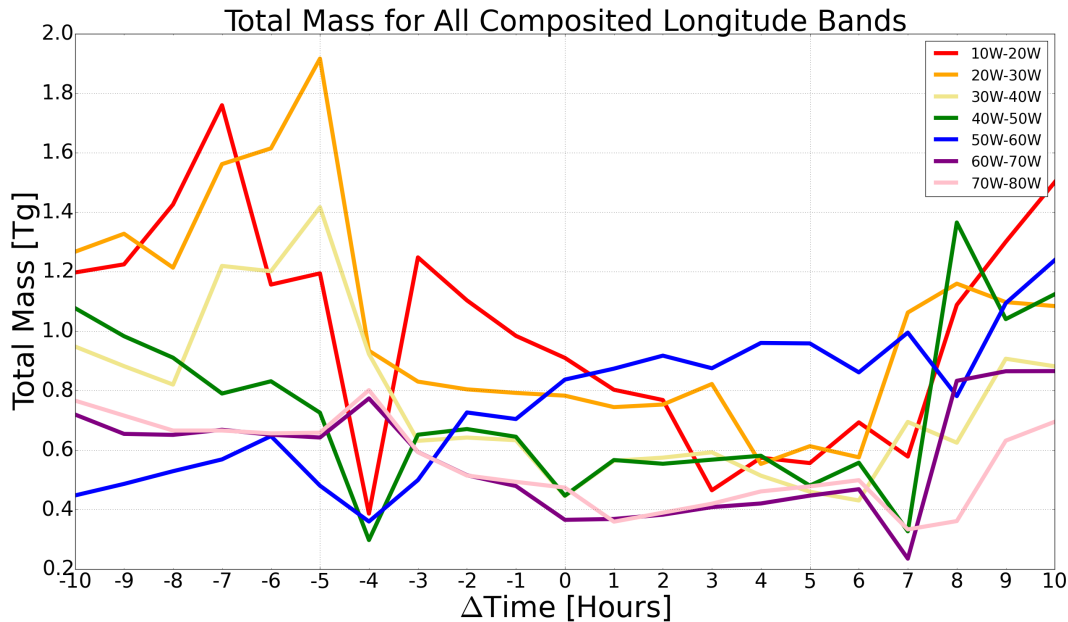
FIGURE 5.4: Total mass in teragrams for each hour before, after and during convective events for all longitude cross sections in Figure 1.3.

7 to 9 hours after convection has been identified, and returns back to the typical dust layer in that particular longitude band. As the longitude band is further away from the dust source, the aerosol optical depth decreases, as seen in the 60°W-70°W and 70°W-80°W composites, although convection still illustrates the same effects on the dust layer as in the longitude bands closest to the Saharan Desert. The 50°W-60°W longitude band has a slightly different structure compared to the other longitude bands, where the higher aerosol optical depth values are in the hours after identified convection. This may be due to sampling, as the total aerosol optical depth and total mass figures in Chapter 3 for this band were quite noisy as well.

The total mass for each longitude band across all times around convection can be computed in a similar manner to the two case studies that were presented in Chapter 4. Figure 1.4
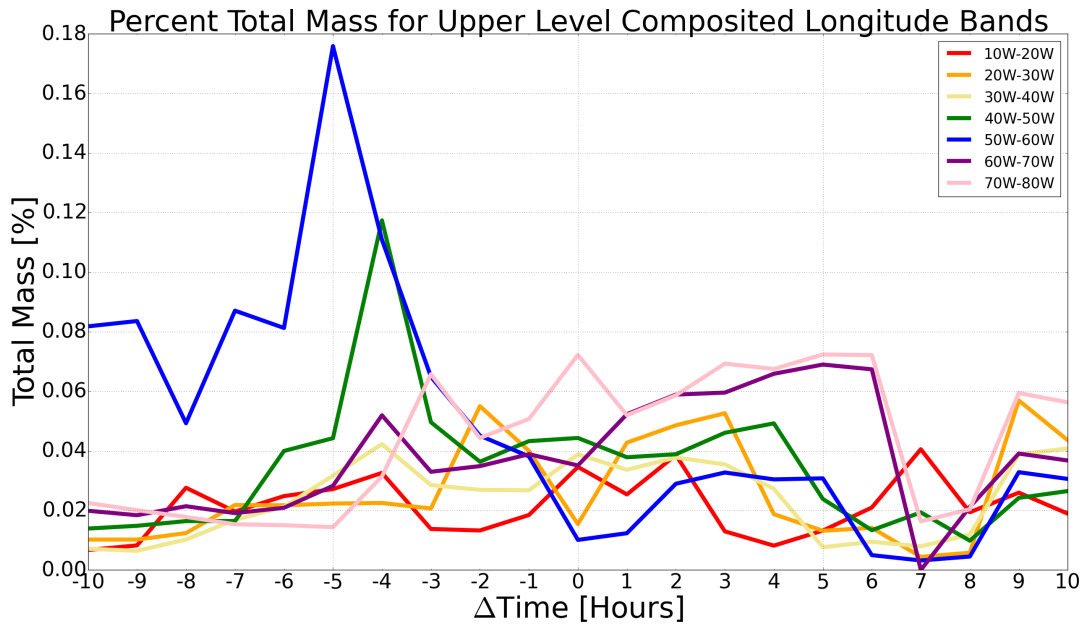
FIGURE 5.5: The percentage of total mass of dust aerosols between 6km and 12km to the total mass of all dust aerosols for all hours in the ten composited longitude cross sections from Figure 1.3.

represents the total mass in teragrams for all longitude bands, and shows how there is a larger amount of aerosol in the hours before convection and then once convection occurs, there is a decrease in total mass. After about 5 to 6 hours after convection, the layers begins to rebuild and the total mass starts to increase, with the longitude bands closest to the dust source having higher total mass values when compared to the longitude bands further away.

Looking at the vertical distribution of the dust layer, the amount of elevated aerosols can be seen when taking the fraction of mass of aerosols above 6km to the total mass. Figure 1.5 shows the percentage of total mass of aerosols at these upper levels for all longitude bands in the domain. The 50°W-60°W band shows a slightly higher percentage in the hours before convection, most likely due to the same sampling issues previously discussed, but the remaining bands show an increase in the percentage between about 3 hours before and 5

hours after convection. This increase at upper levels around convection demonstrates how convection is lofting dust aerosols into the atmosphere not only for the two case studies in Chapter 4, but for convective events in general.

5.2   Convective Impacts

In order to isolate the convective impacts on the dust layer across the tropical Atlantic Ocean, the difference between the full dust layer in a longitude section and the dust layer for when convection was identified can be taken. Figure 1.6 represents what the dust layer looks like for the 20°W-30°W longitude band without isolating convective events. The layer is fairly uniform across all time differences and has a higher aerosol optical depth compared to the convective composites, which is consistent with the characteristics of the dust layer. Although only one longitude band is shown, the remaining bands show the same trend, with the aerosol optical depth decreasing once again as the longitude is further away from the dust source. Taking the difference between the full dust layer and the respective convective composite for each longitude band, the effect of convection can been seen for each band, as shown in Figure 1.7. Blue, positive values indicate where there was a higher aerosol optical depth in the convective composite, where red, negative values represent where the aerosol optical depth was higher in the total dust layer.

For all seven longitude bands, the lower levels, up to about 4km have negative values indicating convection decreased the aerosol optical depth at these levels, particularly in the hours after convection. Hours furthest away from convection generally have lower negative values because
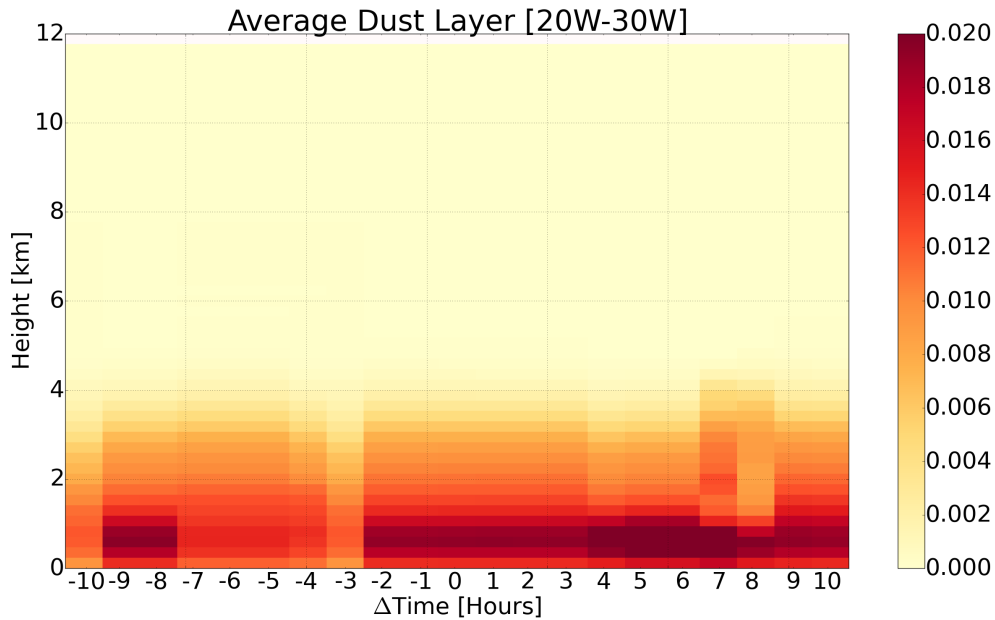
FIGURE 5.6: Vertical distribution of aerosol optical depth for all times from collocated PATMOS-x, CloudSat and CALIPSO observations of the average dust layer without isolating convection for 20°W -30°W.

the dust layer with convective identification has more similar aerosol optical depth values to the total dust layer. Above about 4km, all cross sections have very small positive values, particularly in the hours before convection is identified, representing the additional lofting of aerosols in the convective composites.

To create a better understanding of how convection is altering the dust layer at particular intervals, mass concentrations of before, during and after convective occurrences can be calculated, just as in the two case studies, as well as the difference between during and before convection, after and during convection and before and after convection. Figure 1.8 represents the mass concentration values for the 20°W-30°W longitude band convective composite. Before convection is identified as and average between 3 and 7 hours before convection, during is

63
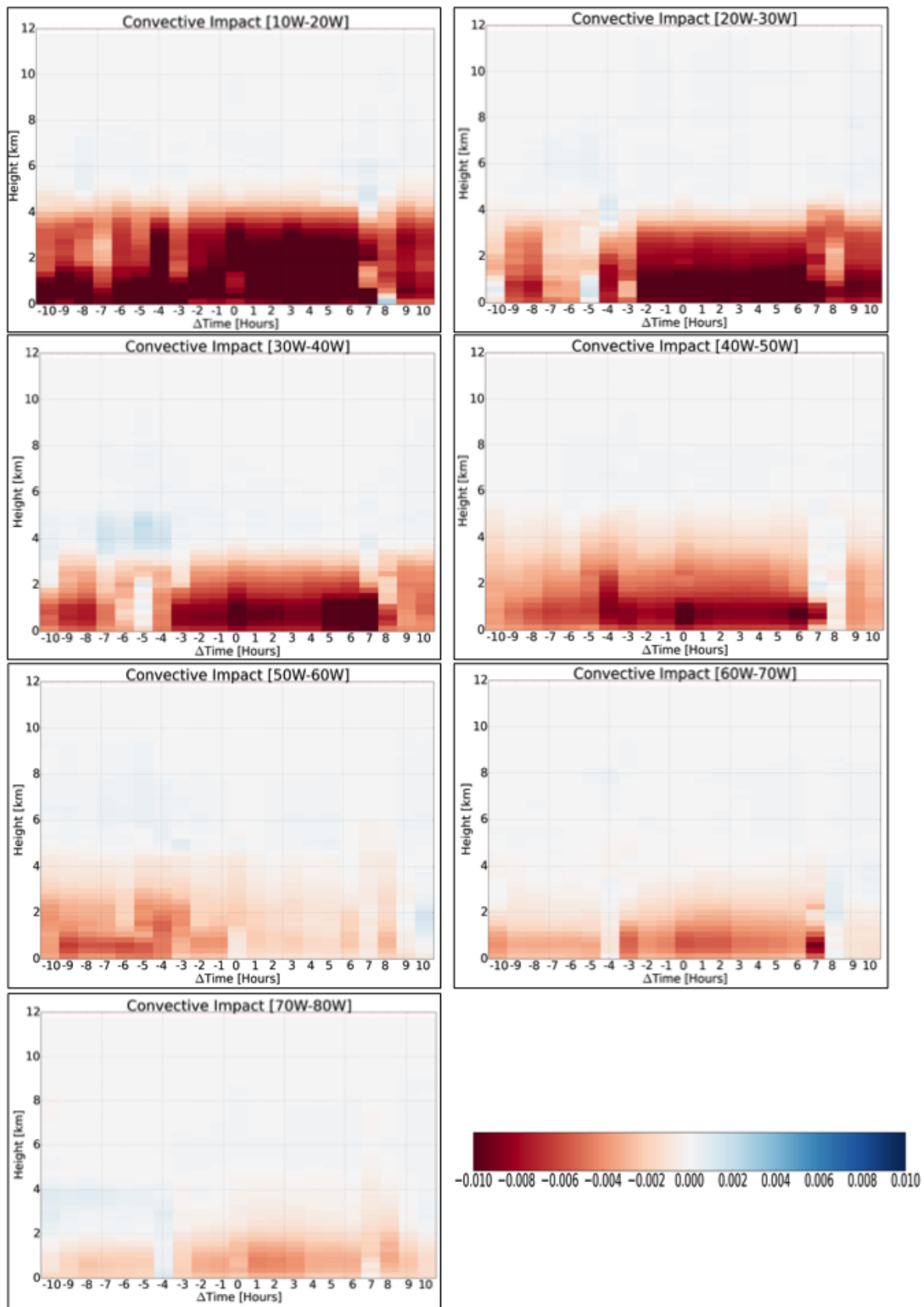
FIGURE 5.7: Composite difference between the average dust layer and identified convection from Figure 1.3 for 10°W-80°W separated into ten degree longitude bands.

an average between 2 hours before and 2 hours after and after convection is represented as an average between 3 hours after and 7 hours after. Panel a, b and c portray the before, during and after convection dust concentration amounts. Of particular interest in these figures are the upper levels of the atmosphere, mainly between 6km and 12km. Before convection, there is a small amount of dust that is located between 6km and 8km, which increases all the way to 12km during convection. Once convection has passed, Panel c hows a decrease in the amount of dust between the entire 6km to 12km region, although there are higher concentrations around the 10km layer showing dust aerosols that stayed lofted in the atmosphere.
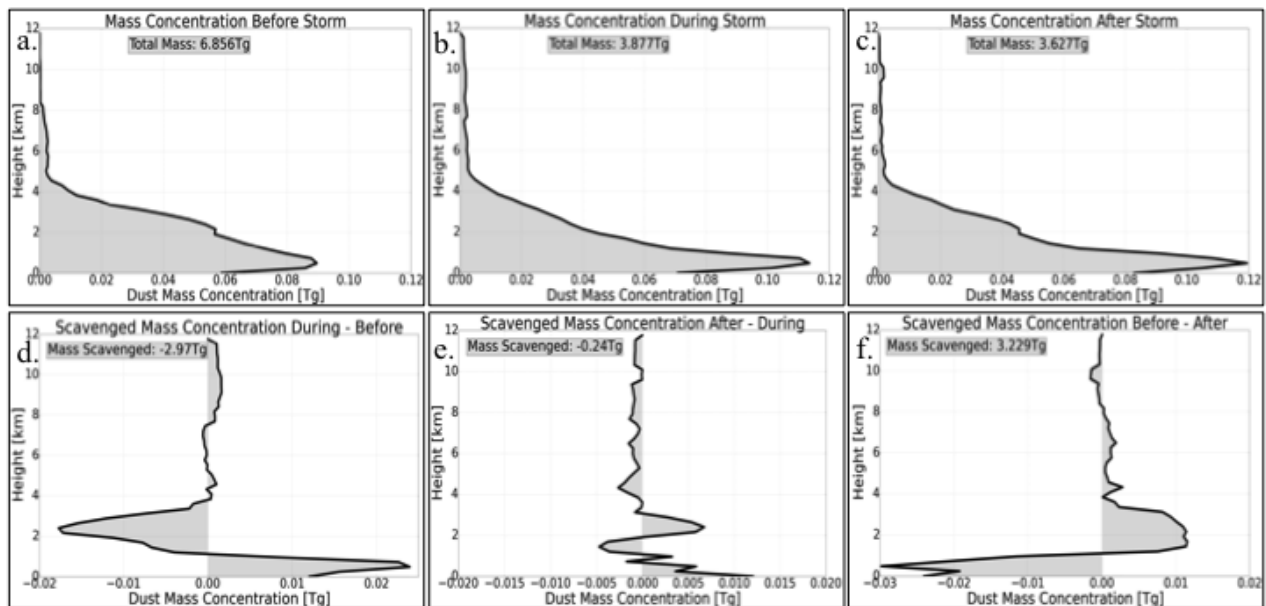
FIGURE 5.8: Dust aerosol mass concentrations for 20°W to 30°W for an average of five hours before, Panel a, during, Panel b, and five hours after, Panel c, convective events are identified. Panels d, e and f represent the difference between during and before, after and during and before and after identified convection to illustrate the effect of convection on the dust layer.

Comparing pre convective and convective dust mass concentrations, Panel d shows how there is a higher concentration of dust at higher layers during convective events, while there is a

higher concentration between 1km and 4km before the convective event occurs. Similarly, Panel e represents the difference in mass concentration after and during convection, where there is more dust aerosol concentration throughout the 4km to 12km column during convection compared to after convection. To understand the effect of convection on the dust layer, Panel f illustrates the difference in dust mass concentration between before and after convective occurrences. This figure is showing how the dust concentration is redistributed from a layer between 1km and 8km before convection, to a small amount of lofted dust between 8km and 12km, as well as at the surface. The aerosol concentration at the surface is most likely due to wet or dry deposition, while the lofted aerosols may be a result of dust that was ingested into the storm and deposited out to upper levels of the atmosphere. Although this explanation is only for one longitude band, the remaining bands have similar results where there is a lofting of aerosols after the storm, in addition to an increased concentration at the surface.

5.3 Discussion

Despite now having a time component added to the dust layer via PATMOS-x cloud properties, there are a few limitations to be aware of when considering the results of the composite analysis. There are two steps that can be taken in order to immediately improve the composite analysis, including using more than four years of data as well as extending the time window around the time of convection. Due to the infrequent 16 day recurring cycle of CloudSat and CALIPSO, there are not a large number of overpasses for four years in a ten degree longitude

band for only when convection is identified, thus limiting the amount of data there is to create a full, complete composite.

A slightly more involved limitation involves the interpolation of the aerosol data through the convective clouds. Since there was not a significantly large amount of data for four years of CloudSat and CALIPSO, the interpolation may have had more of an effect on the results than if there were more years of data being used. By adding more data to the analysis, the potential error may be decreased as there will be more aerosol data to work with. Furthermore, the algorithm that is being used to identify the convection is not free from errors either. Since it is solely using the areal cloud top temperature and cloud optical depth PATMOS-x cloud product data, there may be missed convective cells or falsely identified areas of convection that will slightly skew the results.

Chapter 6

Conclusions and Future Work

6.1 Summary and Discussion

The research objectives proposed in Section 1.4 were focused on interpreting where convective storms and systems redistributed mineral dust in the atmosphere and how convection has changed the vertical distribution of the dust. By first analyzing two separate case studies, Tropical Storm Debby and Hurricane Helene, several science questions were able to be addressed. In both cases, there was lofting of dust aerosol around the convective storms, and evidence of redistribution of the dust through a budget analysis before and after each storm. Additional findings from the budget analysis showed not only a redistribution of dust aerosols from upper to lower layers, but also a thinning of the dust layer after the convective storm moved through a region. In both cases, there was a significant amount of dust that was scavenged away after the storm passed.

Further analyzing the dust layer on a larger scale, the composite analysis over four years for ten hours before and ten hours after identified convection, provided similar results where lofting occurred around the convective storms, and the aerosol optical depth was generally lower after convection was identified.

Understanding the results and findings from this research can help to explain various ambiguities in the climate system that are attributed to mineral dust aerosols. Lofted and redistributed aerosols that were found in the individual case studies, as well as the full composites, can have critical impacts on indirect and direct radiative effects. As the radiative forcing of aerosols is one of the largest uncertainties in predicting global climate change, comprehending this distribution, both vertically and horizontally, of the dust aerosols around convective events can enable an improved representation of the climate system. The knowledge gained from this study of the removal and deposition of dust aerosols will allow insight into the unresolved interactions between clouds and aerosols, therefore contributing to reducing the questionable direction of global climate change.

A key aspect to take away from this work is to recognize the importance of combining several unique datasets together to obtain the most out of the information that is available. With the combined datasets in this work, there is now a time component added to the A-Train polar orbiting satellites, which opens the doors for not only additional mineral dust aerosol research but a variety of other climate related research projects in the future.

6.2   Future Work

6.2.1   Composite Analysis

In addition to the 7 longitude bands that are showing combined daytime and nighttime observations in Chapter 5, daytime and nighttime convective events will be separately analyzed to gain an understanding of how the diurnal cycle plays a role in the redistribution of the dust layer. Convection in this region will most likely have more of an effect on the dust layer at night compared to during the day because of the higher frequency of convective occurrences at nighttime. Nesbitt and Zipser found that rainfall over the oceans peaks in the early morning to predawn hours due to an increase in MCSs observed, while there is a minimum rainfall in the late afternoon, which explains the reduced number of convective occurrences in the daytime observations (Nesbitt and Zipser (2003)).

6.2.2   Connect to Ongoing Modeling and In Situ Data Analyses

As this research project is just one part of a three part study, the results from the satellite observations will be combined with the NAMMA aircraft data and the CSU RAMS model data to gain a full understanding of how convection impacts the dust layer in the tropical Atlantic Ocean. The Regional Atmospheric Modeling System (RAMS) is a cloud-resolving model that resolves convection and will be able to simulate how dust particles behave as CCN and IN, how the dust moves though out the storm and where the particles are deposited after the convection has ceased (Saleeby and van den Heever (2013)). Dust vertical profiles and size distributions will be provided by results from NASA's African Monsoon Multidisciplinary

Analysis (NAMMA) flight campaign, that include a full suite of aerosol and cloud physics instrumentation. This combination of cloud resolving models, remote-sensing and aircraft data is a powerful, unified dataset that will provide the ability to answer the research questions first proposed in Section 1.4 by allowing for the understanding of how much dust is removed from the atmosphere and deposited into the ocean, and how the vertical distribution of dust is altered, relative to pre storm amounts.

6.2.3   Pursue Elevated Dust Layers

With the identification of elevated dust aerosols at multiple levels in the atmosphere, additional analyses must be completed to fully understand how and why the aerosols are being elevated and what environmental impacts these elevated layers will have. Environmental variables such as vertical motion will be explored to find relationships between the lofted aerosols and deposition rates across the tropical Atlantic Ocean. Monthly averages of vertical motion will be compared to the convective fraction from CloudSat and PATMOS-x as well as GPCP rainfall data to find correlations between deposition rates and rainfall.

6.2.4   Improving Procedure for Identifying Convection

In order to decrease the amount of false identifications of convection in the PATMOS-x precipitation algorithm that was created, a more objective approach to identifying convection will be implemented. Using a cluster analysis to identify convection and the other precipitation categories defined in Section 3.4, will allow for parameters that are similar to each other to be grouped together as opposed to the hard thresholds that are currently in place. The cluster

analysis will also be able to further separate convection into multiple size categories to then perceive how larger or smaller convective storms impact the dust layer.

6.2.5 Radiative Impacts and Ocean Fertilization

Once the convective algorithm is created using the cluster analysis, an analysis on how the removal and redistribution of dust impacts ocean fertilization, as well as the indirect and direct radiative effects both locally and downstream of the convective storm development. MODIS data will be used in combination with CALIPSO data to not only evaluate the horizontal and vertical distribution of the dust layer with respect to convective activity, but also to explore the potential impacts of convection on ocean productivity. If there are relationships that are found between ocean productivity and convective activity, assessments can be made as to whether or not ocean color change is a result of wet deposition providing nutrients from the atmosphere. The combined CloudSat and CALIPSO radiative fluxes and heating rates product will be able to provide the information needed to investigate the radiative changes.

6.2.6 Refining Global Models

Global models are greatly in need of observational data to increase their performance. The Community Earth System Model (CESM) is a fully-coupled global climate model that provides state of the art simulated data on Earths past, present and future climate states (Kay et al., 2015). A planned trip to the National Center for Atmospheric Research (NCAR) will allow for the integration of the results of dust transport from these observations into the model. This combination will allow the model to better produce dust transport results in the

tropical Atlantic Ocean, and grant an improved understanding from the model of the climatic

effects due to dust aerosols.

Bibliography

Alcala, C. M. and A. E. Dessler, 2002: *Observations of deep convection in the tropics using the Tropical Rainfall Measuring Mission (TRMM) precipitation radar*, Vol. 107.D24. Journal of Geophysical Research: Atmospheres.

Andreae, M. O., D. Rosenfeld, P. Artaxo, A. Costa, G. Frank, K. Longo, and M. Silva-Dias, 2004: Smoking rain clouds over the amazon. *Science*, **303 (5662)**, 1337–1342.

Arkin, P. and B. Meisner, 1987: The relationship between large-scale convective rainfall and cold cloud over the western hemisphere during 1982-84. *Monthly weather review*, **115 (1)**, 51–74.

Arkin, P. A., 1979: The relationship between fractional coverage of high cloud and rainfall accumulations during gate over the b-scale array. *Monthly Weather Review*, **107 (10)**, 1382–1387.

Beyer, H. G., et al., 2004: Assessing satellite derived irradiance information for south america within the unep resource assessment project swera. *Proceedings of 5th ISES Europe Solar Conference in Freiburg, Germany.*

Burton, S., et al., 2010: Using airborne high spectral resolution lidar data to evaluate combined active plus passive retrievals of aerosol extinction profiles. *Journal of Geophysical Research: Atmospheres*, **115 (D4)**.

Carrio, G. and W. Cotton, 2011: Investigations of aerosol impacts on hurricanes: Virtual seeding flights. *Atmospheric Chemistry and Physics*, **11 (6)**, 2557–2567.

Chen, G., et al., 2011: Observations of saharan dust microphysical and optical properties from the eastern atlantic during namma airborne field campaign. *Atmospheric Chemistry and Physics*, **11 (2)**, 723–740.

Clark, J. D., 1983: The goes user's guide. *NASA STI/Recon Technical Report N*, **83**, 31 710.

DeMott, P. J., K. Sassen, M. R. Poellot, D. Baumgardner, D. C. Rogers, S. D. Brooks, A. J. Prenni, and S. M. Kreidenweis, 2003: African dust aerosols as atmospheric ice nuclei. *Geophysical Research Letters*, **30 (14)**.

DeMott, P. J., et al., 2010: Predicting global atmospheric ice nuclei distributions and their impacts on climate. *Proceedings of the National Academy of Sciences*, **107 (25)**, 11 217–11 222.

Dunion, J. P. and C. S. Velden, 2004: The impact of the saharan air layer on atlantic tropical cyclone activity. *Bulletin of the American Meteorological Society*, **85 (3)**, 353–365.

Evan, A. T., J. Dunion, J. A. Foley, A. K. Heidinger, and C. S. Velden, 2006: New evidence for a relationship between atlantic tropical cyclone activity and african dust outbreaks. *Geophysical Research Letters*, **33 (19)**.

Fu, R., A. D. Del Genio, and W. B. Rossow, 1990: Behavior of deep convective clouds in the tropical pacific deduced from isccp radiances. *Journal of climate*, **3 (10)**, 1129–1152.

Fung, I. Y., S. K. Meyn, I. Tegen, S. C. Doney, J. G. John, and J. K. Bishop, 2000: Iron supply and demand in the upper ocean. *Global Biogeochem. Cycles*, **14 (1)**, 281–295.

Heidinger, A. K., A. T. Evan, M. J. Foster, and A. Walther, 2012: A naive bayesian cloud-detection scheme derived from calipso and applied within patmos-x. *Journal of Applied Meteorology and Climatology*, **51 (6)**, 1129–1144.

Heidinger, A. K., M. J. Foster, A. Walther, and X. Zhao, 2014: The pathfinder atmospheres-extended avhrr climate dataset. *Bulletin of the American Meteorological Society*, **95 (6)**, 909–922.

Herbener, S. R., S. C. Van Den Heever, G. G. Carrió, S. M. Saleeby, and W. R. Cotton, 2014: Aerosol indirect effects on idealized tropical cyclone dynamics. *Journal of the Atmospheric Sciences*, **71 (6)**, 2040–2055.

Houze, R. A., 2004: Mesoscale convective systems. *Reviews of Geophysics*, **42 (4)**.

Houze Jr, R. A., 2014: *Cloud dynamics*, Vol. 104. Academic press.

Houze Jr, R. A. and C.-P. Cheng, 1977: Radar characteristics of tropical convection observed during gate: Mean properties and trends over the summer season. *Monthly Weather Review*, **105 (8)**, 964–980.

Im, E., C. Wu, and S. L. Durden, 2005: Cloud profiling radar for the cloudsat mission. *Radar Conference, 2005 IEEE International*, IEEE, 483–486.

Jenkins, G. S., A. S. Pratt, and A. Heymsfield, 2008: Possible linkages between saharan dust and tropical cyclone rain band invigoration in the eastern atlantic during namma-06. *Geophysical Research Letters*, **35 (8)**.

Karyampudi, V. M. and T. N. Carlson, 1988: Analysis and numerical simulations of the saharan air layer and its effect on easterly wave disturbances. *Journal of the Atmospheric Sciences*, **45 (21)**, 3102–3136.

Kaufman, Y., I. Koren, L. Remer, D. Tanré, P. Ginoux, and S. Fan, 2005: Dust transport and deposition observed from the terra-moderate resolution imaging spectroradiometer (modis) spacecraft over the atlantic ocean. *Journal of Geophysical Research: Atmospheres*, **110 (D10)**.

Kay, J., et al., 2015: The community earth system model (cesm) large ensemble project: A community resource for studying climate change in the presence of internal climate variability. *Bulletin of the American Meteorological Society*, **96 (8)**, 1333–1349.

Khain, A., D. Rosenfeld, and A. Pokrovsky, 2005: Aerosol impact on the dynamics and microphysics of deep convective clouds. *Quarterly Journal of the Royal Meteorological Society*, **131 (611)**, 2639–2663.

Klüser, L. and T. Holzer-Popp, 2010: Relationships between mineral dust and cloud properties in the west african sahel. *Atmospheric Chemistry and Physics*, **10 (14)**, 6901–6915.

Klüser, L., D. Rosenfeld, A. Macke, and T. Holzer-Popp, 2008: Observations of shallow convective clouds generated by solar heating of dark smoke plumes. *Atmospheric Chemistry and Physics*, **8 (10)**, 2833–2840.

Koren, I., Y. J. Kaufman, R. Washington, M. C. Todd, Y. Rudich, J. V. Martins, and D. Rosenfeld, 2006: The bodélé depression: a single spot in the sahara that provides most of the mineral dust to the amazon forest. *Environmental Research Letters*, **1 (1)**, 014 005.

L'Ecuyer, T. S., W. Berg, J. Haynes, M. Lebsock, and T. Takemura, 2009: Global observations of aerosol impacts on precipitation occurrence in warm maritime clouds. *Journal of Geophysical Research: Atmospheres*, **114 (D9)**.

Liu, D., Y. Wang, Z. Wang, and J. Zhou, 2012: The three-dimensional structure of transatlantic african dust transport: A new perspective from calipso lidar measurements. *Advances in Meteorology*, **2012**.

Liu, D., Z. Wang, Z. Liu, D. Winker, and C. Trepte, 2008: A height resolved global view of dust aerosols from the first year calipso lidar measurements. *Journal of Geophysical Research: Atmospheres*, **113 (D16)**.

Maddox, R. A., 1980: Mesoscale convective complexes. *Bulletin of the American Meteorological Society*, **61**, 1374.

Mahowald, N. M., et al., 2010: Observed 20th century desert dust variability: impact on climate and biogeochemistry. *Atmospheric Chemistry and Physics*, **10 (22)**, 10 875–10 893.

Mapes, B. E., 1993: Gregarious tropical convection. *Journal of the atmospheric sciences*, **50 (13)**, 2026–2037.

Mapes, B. E. and R. A. Houze Jr, 1993: Cloud clusters and superclusters over the oceanic warm pool. *Monthly Weather Review*, **121 (5)**, 1398–1416.

Martin, J. H., M. Gordon, and S. E. Fitzwater, 1991: The case for iron. *Limnology and Oceanography*, **36 (8)**, 1793–1802.

Martin, J. H. and R. M. Gordon, 1988: Northeast pacific iron distributions in relation to phytoplankton productivity. *Deep Sea Research Part A. Oceanographic Research Papers*, **35 (2)**, 177–196.

Masunaga, H., 2012: A satellite study of the atmospheric forcing and response to moist convection over tropical and subtropical oceans. *Journal of the Atmospheric Sciences*, **69 (1)**, 150–167.

Moore, J. K., S. C. Doney, and K. Lindsay, 2004: Upper ocean ecosystem dynamics and iron cycling in a global three-dimensional model. *Global Biogeochemical Cycles*, **18 (4)**.

Moore, J. K., S. C. Doney, K. Lindsay, N. Mahowald, and A. F. Michaels, 2006: Nitrogen fixation amplifies the ocean biogeochemical response to decadal timescale variations in mineral dust deposition. *Tellus B*, **58 (5)**, 560–572.

Nesbitt, S. W. and E. J. Zipser, 2003: The diurnal cycle of rainfall and convective intensity according to three years of trmm measurements. *Journal of Climate*, **16 (10)**, 1456–1475.

Omar, A. H., et al., 2009: The calipso automated aerosol classification and lidar ratio selection algorithm. *Journal of Atmospheric and Oceanic Technology*, **26 (10)**, 1994–2014.

Perry, K. D., T. A. Cahill, R. A. Eldred, D. D. Dutcher, and T. E. Gill, 1997: Long-range transport of north african dust to the eastern united states. *Journal of Geophysical Research: Atmospheres*, **102 (D10)**, 11 225–11 238.

Pili, P., 2000: Calibration of seviri. *Proc. 2000 EUMETSAT Meteorological Satellite Data Users? Conf*, 33–39.

Prospero, J. M. and R. T. Nees, 1977: Dust concentration in the atmosphere of the equatorial north atlantic: Possible relationship to the sahelian drought. *Science*, **196 (4295)**, 1196–1198.

Quijano, A. L., I. N. Sokolik, and O. B. Toon, 2000: Radiative heating rates and direct radiative forcing by mineral dust in cloudy atmospheric conditions. *Journal of Geophysical Research: Atmospheres*, **105 (D10)**, 12 207–12 219.

Ramanathan, V., P. Crutzen, J. Kiehl, and D. Rosenfeld, 2001: Aerosols, climate, and the hydrological cycle. *science*, **294 (5549)**, 2119–2124.

Richards, F. and P. Arkin, 1981: On the relationship between satellite-observed cloud cover and precipitation. *Monthly Weather Review*, **109 (5)**, 1081–1093.

Rodríguez, S., et al., 2011: Transport of desert dust mixed with north african industrial pollutants in the subtropical saharan air layer. *Atmospheric Chemistry and Physics Discussions*, **11 (3)**, 8841–8892.

Rosenfeld, D., Y. Rudich, and R. Lahav, 2001: Desert dust suppressing precipitation: A possible desertification feedback loop. *Proceedings of the National Academy of Sciences*, **98 (11)**, 5975–5980.

Saleeby, S. M. and S. C. van den Heever, 2013: Developments in the csu-rams aerosol model: Emissions, nucleation, regeneration, deposition, and radiation. *Journal of Applied Meteorology and Climatology*, **52 (12)**, 2601–2622.

Schmetz, J., P. Pili, S. Tjemkes, D. Just, J. Kerkmann, S. Rota, and A. Ratier, 2002a: An introduction to meteosat second generation (msg). *Bulletin of the American Meteorological Society*, **83 (7)**, 977–992.

Schmetz, J., P. Pili, S. Tjemkes, D. Just, J. Kerkmann, S. Rota, and A. Ratier, 2002b: Seviri calibration. *Bull. Am. Meteorol. Soc*, **83**.

Smalley, M., T. L'Ecuyer, M. Lebsock, and J. Haynes, 2014: A comparison of precipitation occurrence from the ncep stage iv qpe product and the cloudsat cloud profiling radar. *Journal of Hydrometeorology*, **15 (1)**, 444–458.

Sokolik, I., et al., 2001: Introduction to special section: Outstanding problems in quantifying the radiative impacts of mineral dust. *Journal of Geophysical Research: Atmospheres*, **106 (D16)**, 18 015–18 027.

Stephens, G. L., et al., 2002: The cloudsat mission and the a-train: A new dimension of space-based observations of clouds and precipitation. *Bulletin of the American Meteorological Society*, **83 (12)**, 1771–1790.

Sun, B., M. Free, H. L. Yoo, M. J. Foster, A. Heidinger, and K.-G. Karlsson, 2015: Variability and trends in us cloud cover: Isccp, patmos-x, and clara-a1 compared to homogeneity-adjusted weather observations. *Journal of Climate*, **28 (11)**, 4373–4389.

Tegen, I. and I. Fung, 1994: Modeling of mineral dust in the atmosphere: Sources, transport, and optical thickness. *Journal of Geophysical Research: Atmospheres*, **99 (D11)**, 22 897–22 914.

Tobin, I., S. Bony, and R. Roca, 2012: Observational evidence for relationships between the degree of aggregation of deep convection, water vapor, surface fluxes, and radiation. *Journal of Climate*, **25 (20)**, 6885–6904.

Twohy, C. H., 2015: Measurements of saharan dust in convective clouds over the tropical eastern atlantic ocean*. *Journal of the Atmospheric Sciences*, **72 (1)**, 75–81.

Twomey, S., 1974: Pollution and the planetary albedo. *Atmospheric Environment (1967)*, **8 (12)**, 1251–1256.

Vaughan, M. A., et al., 2009: Fully automated detection of cloud and aerosol layers in the calipso lidar measurements. *Journal of Atmospheric and Oceanic Technology*, **26 (10)**, 2034–2050.

Walther, A. and A. K. Heidinger, 2012: Implementation of the daytime cloud optical and microphysical properties algorithm (dcomp) in patmos-x. *Journal of Applied Meteorology and Climatology*, **51 (7)**, 1371–1390.

Walther, A., A. K. Heidinger, and S. Miller, 2013: The expected performance of cloud optical and microphysical properties derived from suomi npp viirs day/night band lunar reflectance. *Journal of Geophysical Research: Atmospheres*, **118 (23)**.

Williams, M. and R. A. Houze Jr, 1987: Satellite-observed characteristics of winter monsoon cloud clusters. *Monthly Weather Review*, **115 (2)**, 505–519.

Winker, D. M., J. R. Pelon, and M. P. McCormick, 2003: The calipso mission: Spaceborne lidar for observation of aerosols and clouds. *Third International Asia-Pacific Environmental Remote Sensing Remote Sensing of the Atmosphere, Ocean, Environment, and Space*, International Society for Optics and Photonics, 1–11.

Winker, D. M., M. A. Vaughan, A. Omar, Y. Hu, K. A. Powell, Z. Liu, W. H. Hunt, and S. A. Young, 2009: Overview of the calipso mission and caliop data processing algorithms. *Journal of Atmospheric and Oceanic Technology*, **26 (11)**, 2310–2323.

Yu, H., M. Chin, D. M. Winker, A. H. Omar, Z. Liu, C. Kittaka, and T. Diehl, 2010: Global view of aerosol vertical distributions from calipso lidar measurements and gocart simulations: Regional and seasonal variations. *Journal of Geophysical Research: Atmospheres*, **115 (D4)**.

Zipser, E. J., et al., 2009: The saharan air layer and the fate of african easterly waves?nasa's amma field study of tropical cyclogenesis. *Bulletin of the American Meteorological Society.*